4

Electrostatic Force Microscopy and Kelvin Force Microscopy as a Probe of the Electrostatic and Electronic Properties of Carbon Nanotubes

Thierry Mélin, Mariusz Zdrojek, and David Brunel

Summary. This chapter addresses recent experimental studies on carbon nanotubes and nanotube devices using electrical techniques derived from atomic force microscopy. Electrostatic force microscopy (EFM), Kelvin force microscope (KFM), and their variants are introduced. We show how EFM-related techniques are used to image the electrostatic and electronic properties of individual carbon nanotubes on insulators, to manipulate their charge state, and to measure field-emission and band-structure properties of individual nanotubes. We then describe how KFM-related techniques can bring insight into the operation of electronic devices based on carbon nanotubes. We focus here on the case of field effect transistors, and describe how KFM techniques can be used to study charge transfers at the nanotube–contact interfaces, to assess the transport properties in carbon nanotubes, and, finally, to characterize carbon nanotube devices under operation.

Key words: Scanning probe microscopy, electrostatic force microscopy, Kelvin force microscopy, charge detection, carbon nanotubes, carbon nanotube field effect transistor, electrostatics, surface potential measurement.

4.1 Introduction

This chapter consists of a review of recent experimental studies on carbon nanotubes and nanotube devices using electrical techniques derived from atomic force microscopy (AFM). It falls in the conjunction of two recently developed research fields: (1) on the one hand, the field of carbon nanotubes since their discovery by Iijima et al. [1] and the strong interest in the field of nanoelectronics following the first carbon nanotube field effect transistor (CNTFET) [2, 3], and (2) on the other hand, the invention of the scanning tunneling microscope [4] followed by the AFM [5], allowing electrostatic or electronic measurements on insulators at the nanometer scale, either by direct measurement of electrostatic forces [6–9] or by the measurement of local surface potentials [10]. The aim of this chapter is to review the experimental studies

carried out in the intersection of these fruitful domains. This chapter starts with a general introduction about electrostatic force microscopy (EFM) and Kelvin force microscope (KFM) experimental techniques as well as their variants (Sect. 4.2). We describe how these techniques have been used to image the electrostatic properties of carbon nanotubes on insulators (Sect. 4.3), and then how more sophisticated electrostatic experiments have been developed at the scale of single nanotubes, in order to manipulate the charge state of individual nanotubes on insulators (Sect.4.4), or to measure their local electronic and band-structure properties (including semiconducting/metallic characters) (Sect. 4.5). In Sect. 4.6, we address the case of CNTFETs, and especially the study of charge transfers at the nanotube–contact interfaces, the assessment of diffusive or ballistic character of transport along single-walled carbon nanotubes (SWCNTs), and finally, more recent studies performed on carbon nanotube devices under operation.

4.2 Electrostatic Measurements at the Nanometer Scale

This section consists of a review of the main electrical techniques derived from AFM [5], which have been developed to perform electrostatic measurements at the nanometer scale [6–10]. Although all techniques presented here are based on the measurement of electrostatic forces, they strongly differ in their implementations, output signals, advantages, and drawbacks. No standard terminology for these techniques has been clearly used, so that, for instance, in the case of surface potential measurements, nearly identical techniques can be named either Kelvin force microscopy (KFM), surface potential probe microscopy, ac-EFM, or scanning Kelvin force microscopy. The aim of this section is to establish a comprehensive description of these techniques that can be used as a guide to understand the literature and recent developments related to the measurements of the local electrostatic properties of carbon nanotubes and devices based on carbon nanotubes.

4.2.1 Electrostatic Force Microscopy

Principle

EFM is a technique based on the measurement of electrostatic forces gradients. Basically, the force $F(z)$ felt by the cantilever oscillating at a mean distance z_0 from the substrate can be written in a first-order approximation as: $F(z) = F(z_0)+\partial F/\partial z(z_0)\cdot(z-z_0)$. In this expression, $\partial F/\partial z(z_0)$ is the derivative with respect to z of the vertical force on the cantilever tip, also referred to as the "force gradient" acting on the tip (expressed in N m^{-1}). It is equivalent to a modification $-\Delta k$ of the cantilever spring constant, which shifts the resonance eigenfrequency f_0. Using $f_0 = 1/2\pi(k/m)^{1/2}$ (where k is the cantilever spring and m the effective mass of the cantilever), the basic relation between the

cantilever frequency shift Δf and the force gradient $\partial F/\partial z(z_0)$ can be readily obtained:

$$\frac{\Delta f}{f_0} = -\frac{1}{2}\frac{\partial F/\partial z(z_0)}{k} \tag{4.1}$$

Although the minimum detectable force gradient depends on several parameters such as the measurement bandwidth, cantilever temperature, and cantilever quality factor Q_{cant}, and, in some situations, may be limited by the AFM itself (e.g., by the photodiode detector), a practical value for the detectable frequency shifts in typical scanning conditions at atmospheric pressure is of the order of a fraction of 1 Hz, corresponding to $\Delta f/f_0$ as low as a few 10^{-6}, and thus to force gradients less than $10^{-5}\,\text{N m}^{-1}$ for cantilevers with spring constant of a few N m^{-1}, and resonance eigenfrequency f_0 in the 100–300 kHz range. This sensitivity is sufficient to detect a few tens of elementary charges stored in nanostructures, and, in specific cases, enables to observe single charge events at room temperature and atmospheric pressure [11]. The lateral resolution of EFM is, however, in general poorer than the AFM resolution in topography mode because electrostatic forces need to be dissociated from short range surface forces such as repulsive or capillary forces. Hence, in ambient air conditions, the tip is in general lifted from the substrate so as to perform EFM measurements. This limits the lateral resolution down to a few tens of nanometers in ambient air at most, which is, however, sufficient to address and map the electrostatic properties of single nanostructures or nanodevices such as carbon nanotubes or CNTFETs.

Phase Shifts Versus Frequency Shifts

Measurements are generally carried out in a two-step procedure in which each EFM scan line is interleaved between topography scan lines. This enables to define a tip pass in the EFM mode at a controlled distance z over to the substrate plane (*see* Fig. 4.1, *right*). EFM data are recorded with the tip mechanically oscillated in the vicinity of its resonance frequency f_0, and biased at a detection voltage V_{EFM}. Two implementations can then be used. First, the cantilever can be mechanically excited at fixed frequency f_0' close to f_0, and the recorded EFM signal is the phase shift $\Delta\phi$ of the cantilever oscillation. Alternatively, a feedback loop can be introduced that maintains the phase shift $\Delta\phi$ as constant, by adjusting the mechanical excitation frequency f_0'. The EFM signal consists then in the shift Δf of the excitation frequency f_0' necessary to maintain $\Delta\phi$ as constant. Both procedures lead to qualitatively similar images. The phase shift $\Delta\phi$ can be related to Δf a*t the resonance frequency* using $\Delta\phi/2Q_{\text{cant}} = \Delta f/f_0$. However, because of the nonlinearity of the cantilever phase with respect to frequency, this relation no longer holds for large-frequency shifts (i.e., $\Delta f > f_0/2Q_{\text{cant}}$). Frequency shift measurements, which are directly proportional to force gradients, are thus more appropriate than phase shift measurements for quantitative charge imaging purposes.

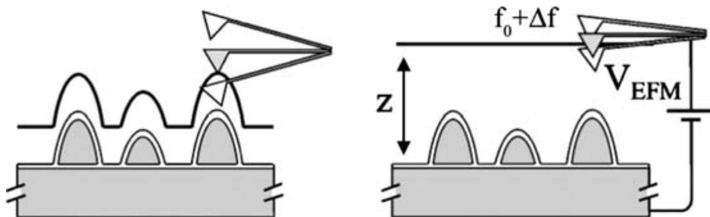

Fig. 4.1. *Left*: Schematics of the topography measurement (here in tapping mode). *Right*: EFM measurement, in which the cantilever is lifted at a distance z above the substrate plane. The cantilever is mechanically excited close to its resonance frequency f_0, and the EFM signal consists in the cantilever eigenfrequency shift Δf (or in the cantilever phase shift $\Delta\phi$, *see* text)

Capacitive Versus Charge EFM Signals

We now treat the case of electrostatic forces involved in EFM signals, by describing the tip-substrate as an ideal capacitance $C(z)$ and introducing a surface potential V_{S} accounting, for example, for the tip-surface work function difference and surface states. Assuming no charge inside the tip-substrate capacitance, the force gradient on the tip is readily expressed as:

$$\frac{\partial F}{\partial z}(z_0) = \frac{1}{2}\frac{\partial^2 C}{\mathrm{d}z^2}(V_{\mathrm{EFM}} - V_{\mathrm{S}})^2 \tag{4.2}$$

Capacitive forces thus lead to negative frequency shifts according to (4.1), varying quadratically as a function of $(V_{\mathrm{EFM}} - V_{\mathrm{S}})$. When a charge Q is now introduced in the tip-substrate capacitance, an effective surface potential V_{Q} proportional to the charge Q builds in,[1] and the total force gradient can now be developed as follows:

$$\frac{\partial F}{\partial z}(z_0) = \frac{1}{2}\frac{\partial^2 C}{\mathrm{d}z^2}[(V_{\mathrm{EFM}} - V_{\mathrm{S}})^2 - 2(V_{\mathrm{EFM}} - V_{\mathrm{S}})V_{\mathrm{Q}} + V_{\mathrm{Q}}^2] \tag{4.3}$$

Two charge contributions thus appear. The first one corresponds to the interaction between charge Q and the charge at the EFM tip apex, and leads to a frequency shift proportional to $(V_{\mathrm{EFM}} - V_{\mathrm{S}}) \cdot V_{\mathrm{Q}}$. The main advantage of this signal is that it enables a determination of the sign of the surface charge Q. The second charge contribution – proportional to Q^2 – corresponds to image charge effects. This component therefore always corresponds to negative frequency shifts (attractive force gradients) and is amplified when scanning over insulating layers [12, 27]. The three electrostatic contributions of EFM signals can be dissociated experimentally by a spectroscopic analysis of EFM signals [13].

[1] V_{Q} depends strictly speaking on the tip surface distance z, while V_{S} would not depend on z, if only related to the tip-substrate work function difference. The determination of V_{Q} as a function Q will not be described here.

Modulated ($1\omega/2\omega$) EFM/FM-KFM

We now describe the case of modulated EFM, also called $1\omega/2\omega$ EFM, in which the EFM static bias is replaced by an ac + dc voltage: $V_{\mathrm{EFM}}(t) = V_{\mathrm{dc}} + V_{\mathrm{ac}} \cos \omega t$, where $\omega << 2\pi f_0$ (quasistatic approximation). The electrostatic force gradient $\partial F/\partial z(z_0)$ now reads: $\partial F/\partial z(z_0) = 1/2\partial^2 C/\partial z^2(V_{\mathrm{dc}} + V_{\mathrm{ac}} \cos \omega t - V_{\mathrm{S}} - V_{\mathrm{Q}})^2$ and hence exhibits one static component and two oscillating components at 1ω and 2ω:

$$\begin{cases} \partial F/\partial z(z_0)|_{0\omega} = 1/2\partial^2 C/\partial z^2[V_{\mathrm{dc}}^2 + V_{\mathrm{ac}}^2/2] \\ \partial F/\partial z(z_0)|_{1\omega} = \partial^2 C/\partial z^2(V_{\mathrm{dc}} - V_{\mathrm{S}}) \cdot V_{\mathrm{ac}} \cos \omega t - \partial^2 C/\partial z^2(V_{\mathrm{Q}} \cdot V_{\mathrm{ac}} \cos \omega t) \\ \partial F/\partial z(z_0)|_{2\omega} = 1/4\partial^2 C/\partial z^2 V_{\mathrm{ac}}^2 \cos 2\omega t \end{cases} \tag{4.4}$$

This shows that provided V_{dc} can be adjusted to V_{S} (e.g., with the tip positioned over the surface), the force gradient component at 1ω measures the interaction between charge Q and ac charges at the EFM tip, whereas the component at 2ω measures capacitive effects. This technique can be employed to record separately charge and capacitive (dielectric) force gradient images, respectively [11]. Alternatively, the introduction of a feedback loop that sets to zero (or "nullifies") the force gradient at 1ω enables to measure the local contact potential difference $V_{\mathrm{S}} + V_{\mathrm{Q}}$, which contains the information about the surface potential and local charge Q. Although this technique is derived from EFM (i.e. based on force gradients), it is also called frequency modulation Kelvin force microscopy (FM-KFM) in noncontact AFM, in analogy with Kelvin force microscopy described hereafter, which enables to measure local surface potentials.

4.2.2 Kelvin Force Microscopy

Principle of Amplitude Modulation Kelvin Force Microscopy

KFM (for a historical reference, *see* [10]) is in its usual implementation on atmospheric pressure AFM, a technique based on the electrostatic excitation of cantilevers – in contrast with EFM in which the cantilever is mechanically excited – and on the nullification of its oscillation amplitude. This technique is thus here based on forces, rather than on force gradients. It is now also called amplitude modulation Kelvin force microscopy, in comparison with FM-KFM based on force gradients (*see* Sect. 4.2.1).

More precisely, the electrostatic excitation is generated by an ac + dc voltage that can be applied either to the substrate, a device, or directly to the EFM tip. In this later option, the ac+dc voltage leads to an electrostatic force $F(z)$ at a distance z from the surface: $F(z) = 1/2\partial C/\partial z(V_{\mathrm{dc}} + V_{\mathrm{ac}} \cos \omega t - V_{\mathrm{S}} - V_{\mathrm{Q}})^2$. Following the development of (4.4), this force splits into one static component and two oscillating components at 1ω and 2ω:

$$\begin{cases} F(z)|_{0\omega} = 1/2\partial C/\partial z[V_{\text{dc}}^2 + V_{\text{dc}}^2/2] \\ F(z)|_{1\omega} = \partial C/\partial z(V_{\text{dc}} - V_{\text{S}}) \cdot V_{\text{ac}} \cos \omega t - \partial C/\partial z V_Q \cdot V_{\text{ac}} \cos \omega t \\ F(z)|_{2\omega} = 1/4\partial C/\partial z(V_{\text{ac}}^2 \cos 2\omega t) \end{cases} \quad (4.5)$$

Here, however, the ac angular frequency is generally set close to the eigenfrequency of the cantilever: $\omega \sim 2\pi f_0$, so that $F(z)|_{0\omega}$ and $F\ (z)|_{2\omega}$ fall out of resonance with the cantilever, whereas $F(z)|_{1\omega}$ leads to an oscillation amplified by the cantilever quality factor Q_{cant} (typically $Q_{\text{cant}} \sim 200$ at atmospheric pressure). A feedback loop is then introduced, so as to nullify the cantilever oscillation amplitude at 1ω, by adjusting the dc component of the electrostatic excitation. From (4.5), this condition is obtained provided $V_{\text{dc}} = V_{\text{S}} + V_{\text{Q}}$, that is, when the dc bias on the tip exactly matches the local surface potential $V_{\text{S}} + V_{\text{Q}}$: KFM therefore enables the real-time measurement and mapping of local surface potentials.

Open-Loop KFM or ac-EFM

This section briefly discusses the case of open-loop KFM measurements, which consist in mapping the cantilever oscillation amplitude at 1ω, when electrostatically excited, but in absence of KFM regulation loop. This technique is used so as to generate an image of the force at 1ω at the tip, proportional to $\partial C/\partial z(V_{\text{dc}} - V_{\text{S}}) \cdot V_{\text{ac}}$ as seen in (4.5). It should be noted that this mode has been applied to carbon nanotubes and carbon nanotube devices [14]. It was then referred to as "ac-EFM," due to the absence of feedback loop measuring the local surface potential, whereas, however, the "ac-EFM" signal is the one of an open-loop KFM mode, that is based on forces, and not on force gradients like in EFM techniques.

4.2.3 Lateral Resolution in EFM and KFM

Side Capacitance Effects

We describe here a difference between EFM and KFM as for quantitative charge and/or surface potential imaging. In both techniques, the actual detection is performed locally, that is not only through a capacitance $C(z)$ between the tip apex and surface, but also through a series of side capacitances $C_{1\text{t}}(\text{z})$, $C_{2\text{t}}(\text{z})$, ..., $C_{\text{it}}(z)$, "seeing" effective surface potentials Φ_i, as described in Fig. 4.2.

In the case of KFM, the nullification of the total force at 1ω at the cantilever in presence of side capacitances leads to the following equation:

$$\partial C/\partial z(V_{\text{dc}} - V_{\text{S}} - V_{\text{Q}}) \cdot V_{\text{ac}} + \sum \partial C_{\text{it}}/\partial z(V_{\text{dc}} - F_i) = 0$$

so that the measured dc component regulated by the KFM loop becomes an average between $(V_{\text{S}} + V_{\text{Q}})$ and the potentials Φ_i seen by side capacitances

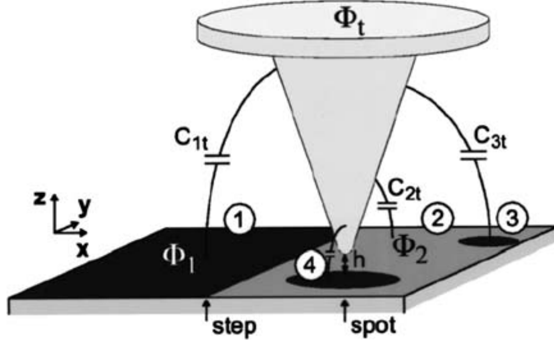

Fig. 4.2. Schematics of the side capacitances C_{1t}, C_{2t}, ..., C_{it} between the cantilever tip and the surface with inhomogeneous local surface potentials Φ_1, ..., Φ_i. Adapted from [15]

C_{it} [15], the relative weight of each of the surface potential Φ_i below the tip being determined by the derivatives of the local capacitances $\partial C/\partial z$ or $\partial C_{it}/\partial z$.

$$V_{dc} = \frac{\partial C/\partial z'(V_S + V_Q) + \sum \partial C_{it}/\partial z' F_i}{\partial C/\partial z + \sum \partial C_{it}/\partial z} \tag{4.6}$$

The assessment of side-capacitance effects is of great importance, for example, for quantitative voltage drop measurements along carbon nanotubes, described later in this chapter. Additionally, one might notice that in the case of EFM or FM-KFM (*see* Sect. 4.2.1), the weights in (4.6) are to be replaced with the second derivatives of the capacitances. This reduces the effects of side-capacitances, due to the increased weight of $\partial^2 C/\partial z^2$ with respect to the sum of the $\partial^2 C_{it}/\partial z^2$ in techniques based on force gradients (i.e., on phase or frequency shifts), as compared with the weight of $\partial C/\partial z$ with respect to the sum of the $\partial C_{it}/\partial z$ in techniques based on the measurement of forces (i.e., on amplitudes).

This lateral resolution effect is illustrated in Fig. 4.3. It shows the topography (Fig. 4.3a) of a connected SWCNT on a SiO_2 surface (*top*), as well as the corresponding EFM image (*middle*, negative EFM tip bias, 3 Hz color scale) and the corresponding KFM image (*bottom*, 200 mV color scale) acquired in similar detection conditions. The nanotube charge environment (here negative) is evidenced by the bright contrast along the nanotube in the EFM image (repulsive interaction between the negative charge in the nanotube environment and the negative charge at the EFM tip) and a dark contrast in the KFM image (negative potential along the nanotube). In addition, a positive local spot of charges has been introduced in the SiO_2 layer in the vicinity of the nanotube by a charge injection technique (to be described later in this chapter), which is monitored as a dark spot in the EFM image (attractive interaction between the positive spot of charges and the negatively biased EFM tip) and as a positive spot in the KFM surface potential image. The

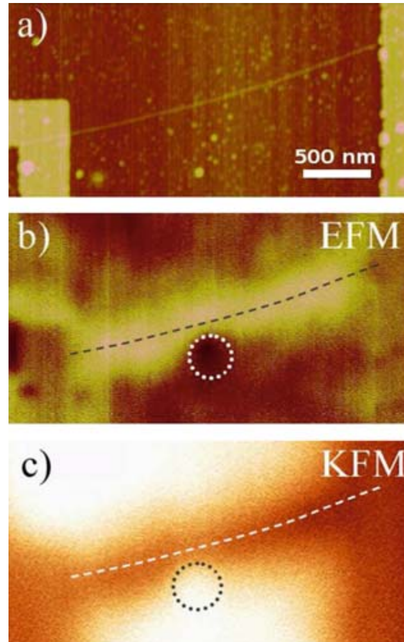

Fig. 4.3. (**a**) Topography image of carbon nanotube field effect transistor (*CNTFET*) (500 nm scale bar). (**b**) EFM image (tip-substrate distance z = 80 nm, $V_{\mathrm{EFM}} = -2$V, 3 Hz color scale) showing (1) the negatively charged environment of the CNTFET channel (bright contrast of the nanotube) and (2) a local spot of positive charge injected in the SiO_2 layer in the vicinity of the nanotube (*dark spot* in the EFM image), serving here as a test bench for the lateral resolution of electrostatic measurements. (**c**) Corresponding KFM image (z = 70 nm, 200 mV color scale), in which the nanotube charged environment corresponds to a negative potential (*dark contrast*) and the local spot of positive charge as a positive potential (*bright contrast*). The difference in lateral resolution in EFM and KFM is visible from (**b**) and (**c**) (*see* text)

difference in lateral resolution between the EFM and the KFM images is obvious from Fig. 4.3b, c, both along the nanotube and for the local spot of charges. The lower lateral resolution in the KFM image illustrates the bigger weight of side capacitance in force techniques compared with force gradient techniques, as explained previously.

Carbon Nanotube Tip Probes

Finally, we also mention the use of carbon nanotube probes for electrostatic (EFM or KFM) measurements. An example of such a probe [16] is given in Fig. 4.4, showing a multiwalled carbon nanotube tip mounted on a standard AFM cantilever tip.

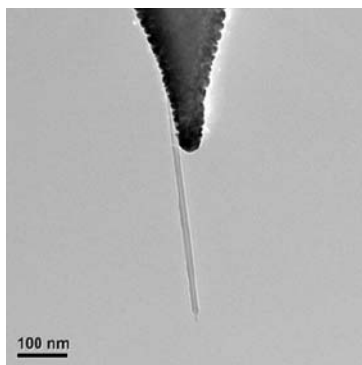

Fig. 4.4. Transmission electron microscopy image of a cantilever tip modified with a glued multiwalled carbon nanotube. Adapted from [16]

As can be obviously seen from Sect. 4.2.3, such a high-aspect ratio tip is ideal to reduce parasitic effects associated with side capacitances, leading to increased lateral resolution, which has been demonstrated in the case of dopant profiling [16], and on contact potential measurements on biased $Al/Al_2O_3/Al$ junctions [17] as well as on bundles of nanotubes [17] or individual MWCNT [18]. This effect is illustrated in the Fig. 4.5, in which the same nanotube has been imaged with a carbon nanotube probe with 200 nm length and $\sim$ 20 nm apex diameter (Fig. 4.5, *left*) and with a conventional Au-plated silicon tip probe (Fig. 4.5, *right*). Although the topography shows a comparable lateral resolution in both cases, the associated KFM images demonstrate the improvement of the lateral resolution using the carbon nanotube tip probe.

4.3 Electrostatic Imaging of Carbon Nanotubes

This section describes the work done on imaging the dielectric properties and native charge in carbon nanotubes using EFM. A large interest has been shown recently on such experiments because EFM can be used to image nanotubes either deposited or directly grown on insulating layers [19–22] or buried inside thin insulating layers [23]. The main physical property imaged in this work is the conductive nature of nanotubes with respect to their insulating environment, giving rise to highly contrasted EFM images, with the possibility to even "reveal" carbon nanotubes not visible in topography images. Hence, EFM had been termed "scanning conductance microscopy" – although no conductance is truly measured, but rather capacitive forces, as explained in Sect. 4.2. This section provides a comprehensive review of these experiments.

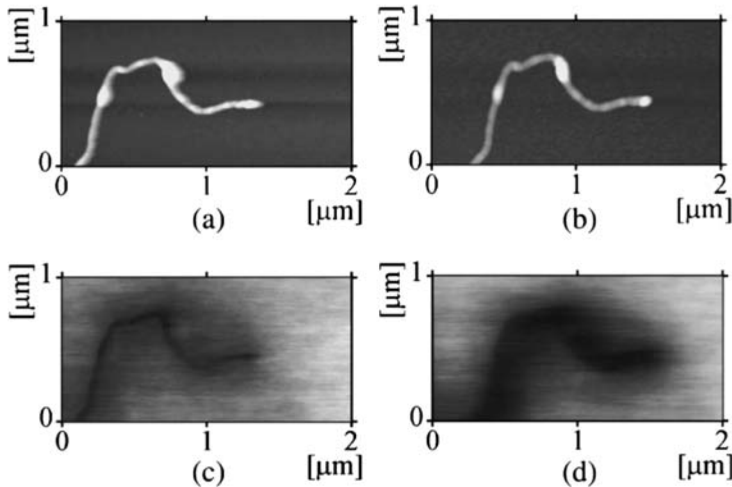

Fig. 4.5. *Top*: Topography of a multiwalled carbon nanotube (diameter ∼ 20 nm) taken with a multiwalled carbon nanotube tip (*left*) and an Au-plated silicon cantilever tip (*right*). *Bottom*: Corresponding KFM images (gray scale ∼ 100 mV), showing an enhanced lateral resolution with the carbon nanotube tip probe. Adapted from [18]

4.3.1 Capacitive Imaging of Carbon Nanotubes in Insulating Layers

The mapping of individual nanotubes buried in thin poly-(methyl methacrylate) (PMMA) films has been reported by Jespersen et al. [23], in a way that illustrates the capacitive detection performed by EFM. Figure 4.6a shows a schematics of the composite sample made of SWCNTs dispersed in PMMA and spin-coated as an ∼ 60 nm-thin film on a SiO_2-covered doped silicon substrate. In addition, it shows the principle of EFM detection, performed in a similar way as described in Sect. 4.2, here, however, using the cantilever phase shift to track electrostatic force gradients. The topography image of the sample is shown in Fig. 4.6b. As nanotubes are buried into the PMMA film, they cannot be revealed from this image that only shows the presence of small particles with height ∼ 10–20 nm, stemming from the carbon nanotube powder dispersed in PMMA. This contrasts with the EFM image (Fig. 4.6c) acquired simultaneously with topography, where single or agglomerated carbon nanotubes can be revealed and imaged as dark lines in the EFM image. The EFM signal stems from the much higher conductance of SWCNT compared with the PMMA matrix, leading to a significant increase of the tip-sample capacitance because of the presence of the carbon nanotube in this capacitance, and, thus, to a cantilever negative phase shift (*see* Sect. 4.2 for details).

The contrast of the EFM image is further analyzed, and shows strong variations in the phase shift amplitude (*see* Fig. 4.7, *left*, for illustration) even

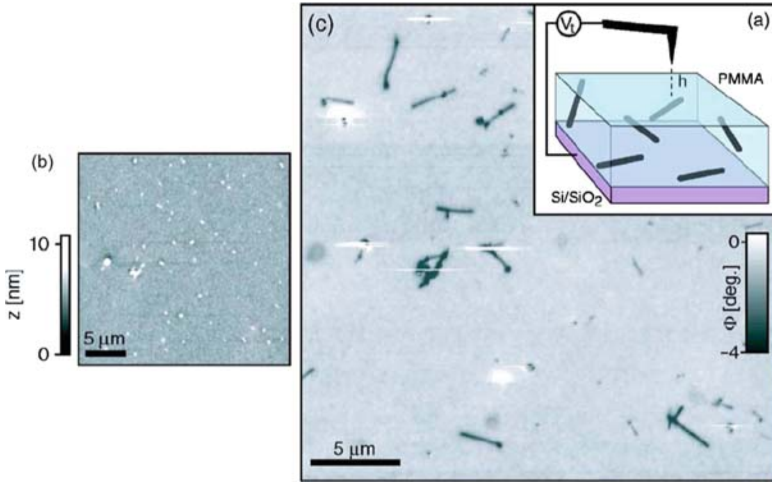

Fig. 4.6. (**a**) Schematic illustration of the polymer/SWCNT sample and EFM operation. (**b**) Topography image of the 60 nm-thick film of PMMA/SWCNT composite. Because of the polymer, the tubes cannot be observed. (**c**) Corresponding EFM image (tip-substrate distance $h = 35$ nm, tip biased at +7 V), in which individual SWCNTs are clearly seen as dark lines (negative phase shifts). Adapted from [23]

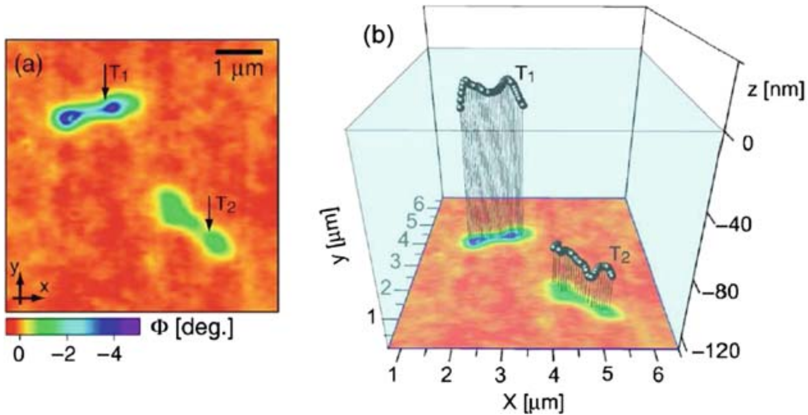

Fig. 4.7. *Left*: EFM image showing two SWCNTs embedded in an ∼ 170 nm-thick film of SWCNT/PMMA composite (5° phase shift color scale). *Right*: Projection view of the three dimensional map of the two nanotubes as inferred from the modeling of EFM signals. The blue region illustrates the PMMA matrix. Adapted from [23]

for nanotubes of similar length. This is explained by the fact that the nanotube can be incorporated in the PMMA matrix either (1) close to the substrate (*see*, e.g., the nanotube labeled T2 in Fig. 4.7) or (2) close to the PMMA layer surface (*see* nanotube T1). This situation is depicted in Fig. 4.7 (*right*), and was quantitatively linked with the EFM image phase shift contrasts associated with the nanotube [23], showing the EFM can both reveal and locate carbon nanotubes in the PMMA matrix, although not visible in topographic images.

4.3.2 EFM Imaging of Carbon Nanotubes and DNA

Another use of EFM to assess the dielectric properties of one-dimensional nanostructures on surfaces is handled in [19], in which the case of SWCNTs and DNA single strands has been debated. The EFM detection is first discussed in the case of SWCNTs on oxide surface with different lengths, as shown in Fig. 4.8. Images with similar contrast as in Fig. 4.6 are obtained, here showing also a dependence on the EFM contrast as a function of the nanotube length L. This is interpreted as stemming from the variation of the nanotube-substrate plane capacitance as a function of the L, leading to the following dependence for the cantilever phase shift $\Delta\phi : (\Delta\phi)^{-1/2} = a + bL^{-1}$ (*see* [19] for details), in agreement with experimental data (*see* Fig. 4.8, *lower inset*).

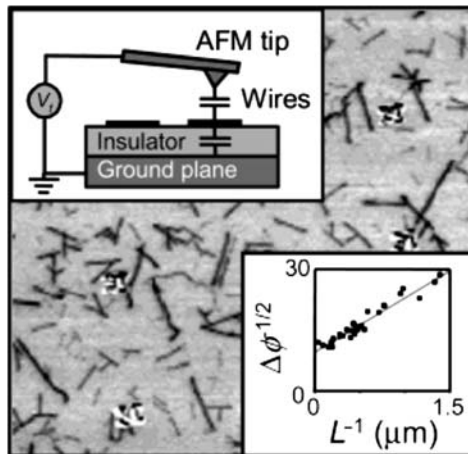

Fig. 4.8. *Upper inset*: experimental setup. An AFM cantilever is driven near its resonance frequency. A "scanned conductance image" is obtained by producing a gray scale plot of the phase shift ϕ of the cantilever as a function of tip position. (*Main panel*) Scanned conductance image for SWCNTs. Dark lines indicate negative phase shifts $\Delta\phi$ occurring when the tip is over a tube. (*Lower inset*) Plot of $\Delta\phi^{-1/2}$ as a function of the inverse tube length L^{-1} for 26 individual tubes. The data follow a straight line (*see* text). Adapted from [19]

The case of SWCNTs is then compared with the case of λ-DNA strands deposited on the same surface. Since both molecules show the same height (∼ 1 nm) in the topography images, the identification of carbon nanotubes and λ-DNA molecules has been carried out by imaging first the topography of a nanotube dispersion on the substrate (data not shown) and then imaging the same surface after λ-DNA deposition using recognition markers predefined by lithography (*see* yellow feature in Fig. 4.9a), enabling an unambiguous identification of the λ-DNA strands.

The topography of the surface is illustrated in Fig. 4.9a, where the λ-DNA molecules are green, and the carbon nanotubes appear in red. A high-resolution $4.5 \times 4.5\,\mu m^2$ zoom of the blue box is shown in Fig. 4.9b, together with the corresponding EFM image in Fig. 4.9c. It is striking in Fig. 4.9c that only the capacitive features associated with the carbon nanotubes can be

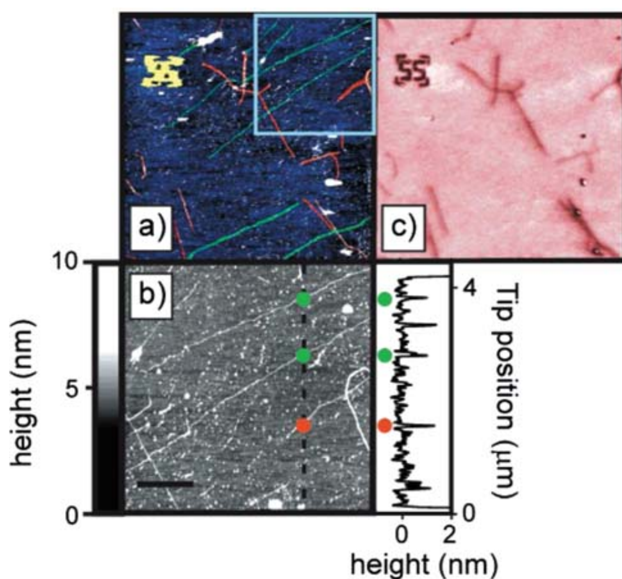

Fig. 4.9. (**a**) Colorized topographic image of SWCNT bundles and single tubes, colored red, and λ-DNA molecules, colored green. A 1 μm alignment mark is shown in yellow. (**b**) $4.5 \times 4.5\,\mu m^2$ topographic scan of the region enclosed by the *blue square* in (**a**). The higher resolution scan shows the topographic features more clearly than it is possible with the larger area scan in (**a**). The gray level scale is shown to the immediate left of the image. The scale bar is 1 μm. A SWCNT is marked by a *red dot*, whereas two λ-DNA molecules are marked by *green dots*. The graph to the immediate right of the panel shows a line trace through the topographic image along the *dotted line*, with a constant offset height subtracted from the data. Both the SWCNT and λ-DNA molecules are ∼ 1 nm in height. (**c**) EFM image of the region shown in part (**a**). Although the SWCNT and the λ-DNA are similar in height, no signal appears in the EFM image when the tip is over the λ-DNA molecules. Adapted from [19]

seen in the EFM image, whereas λ-DNA strands cannot be resolved. This was interpreted as a proof that λ-DNA molecules consist in an electrical insulator with an extremely low conductivity, in contrast with SWCNTs[2] [19].

4.3.3 Imaging of Native Charges in Carbon Nanotube Loops

Native charges have been observed in the environment of SWCNTs directly grown by chemical vapor deposition on SiO_2 surfaces, and more precisely when the nanotubes are forming coils on the surface [21]. This is illustrated in Fig. 4.10a, for which an EFM image is displayed with a negative bias V_S applied to the sample. This image shows the usual capacitive footprint of the nanotube topography [here the topography is not shown, *see* [21] for details], appearing as a negative cantilever phase shift. The striking feature here is the appearance of a homogeneous negative phase shift signals associated with some of the carbon nanotube coils, such as those selected in Fig. 4.10. This signal corresponds to an attractive force, and thus, due to $V_S < 0$, to a negative charge stored in the coil, with density in the range of a few -10^{-8} C m^{-2}, that is $\sim 10^3$ electrons stored in a loop with $\sim 1\,\mu$m radius. Those charges were

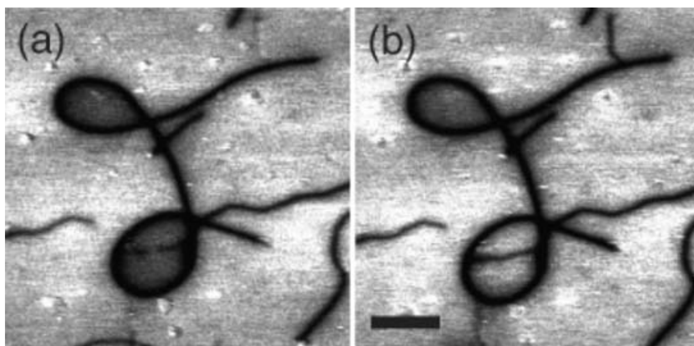

Fig. 4.10. (**a**) EFM image of two loops formed on the same single-walled nanotube, each trapping charges as seen by the phase difference measured in their interior. (**b**) EFM image of same area as (**a**) after touching the interior of the lower loop by the grounded AFM-tip. All measurements were performed with $z = 60$ nm and negative substrte bias $V_S = -6$ V. The scale bar is $2\,\mu$m. Adapted from [21]

[2] Although this work brought a spectacular scanning-probe insight in the debate about the DNA conductivity, it should be nonetheless mentioned that (1) EFM experiments do not rigorously bring information about conductance, but rather about the polarisability (dielectric constant) of the molecules; and (2) the above analysis should be only valid when the charge environment of the nanotube or DNA molecules are evaluated, since EFM is also sensitive to local charges, as shown in Sect. 4.2. This is especially relevant for DNA deposited on insulators, for which a positive charge is found in the surrounding of the DNA ropes [25]. This point is also likely to strongly depend on preparation protocols.

attributed to a native charging of the sample silicon dioxide inside the coils after growth. Moreover, it was shown possible to remove the coil charge by bringing the grounded tip in contact with the inside of the coil (*see* Fig. 4.10a, b for a comparison). Since the charges were uniformly distributed within the loops, this also suggests that the charges are relatively mobile on the surface and not trapped deeply in the substrate, in such type of samples.

4.4 Charge Injection Experiments in Carbon Nanotubes

The results described earlier demonstrate the relevance of electrical techniques derived from AFM to establish the local electrostatic properties of individual nanotubes on insulating layers, and already put forward the interplay between their dielectric and charging properties. It is the aim of this section to develop these aspects, based on experiments that manipulate the charge state of individual carbon nanotubes, that is charge injection experiments. First, we describe the charge injection technique, then we illustrate EFM signals, and finally, we review the properties of charged carbon nanotubes: charging of individual carbon nanotubes and nanotube networks, field-emission properties from charged nanotubes, charging mechanisms and inner-shell charging in the case of MWCNT, and finally, charge enhancements at the nanotube caps, associated with Coulomb repulsion.

4.4.1 Charge Injection and Detection Techniques

Charge injection and detection experiments are typically conducted as follows, using standard AFMs with EFM modes in ambient air (here Multimode/Nanoscope IIIA or Dimension/Nanoscope IV microscopes from Veeco Instruments, Santa Barbara, US). First, the microscope is placed under a dry nitrogen atmosphere in order to avoid (1) charge leakage due to adsorbed surface water and (2) anodic oxidation during the charge injection experiments. Commercial Pt-Ir-coated cantilevers with $\sim 60\,\mathrm{kHz}$ resonance frequency and with low (1–$3\,\mathrm{N\,m^{-1}}$) spring constants are used, so as to address single nanotubes in contact mode, but also to facilitate EFM detection (i.e., cantilever phase or frequency shifts).

Charging experiments are achieved by first localizing individual CNTs from the sample topography acquired in intermittent contact mode AFM. The simplest implementation for charge injection into a given nanotube is to use local approach-retract curves with the EFM cantilever biased at an injection voltage V_{inj} (typically $V_{\mathrm{inj}} = -2$ up to $-12\,\mathrm{V}$) with respect to the sample substrate [12, 25, 27]. In this process, the distance z between the biased EFM tip and the substrate is periodically swept ($\sim 1\,\mathrm{Hz}$ sweep rate), and its minimum value is tuned in order to reach a permanent contact regime between the EFM tip and the CNT (*see* Fig. 4.11) during the z-sweep. In this regime, the cantilever oscillation amplitude becomes zero, and a cantilever quasistatic

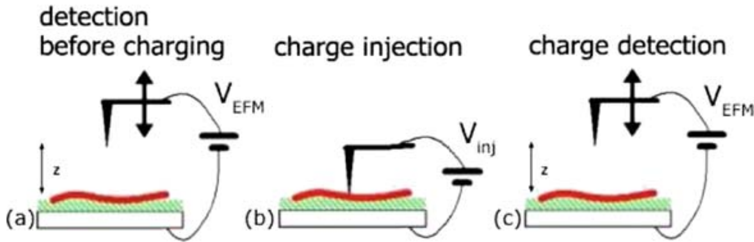

Fig. 4.11. Schematics of the charge injection and detection technique. (**a**) EFM data acquired before charge injection. The recorded EFM signal is the cantilever resonance frequency shift when the tip is biased at V_{EFM} and scanned at a constant distance z above the sample. (**b**) Charge injection with the tip in contact with the nanotube and biased at V_{inj} with respect to the substrate. (**c**) EFM data acquisition after injection. Adapted from [12]

deflection is monitored. This enables to adjust the tip-CNT contact force (here a few nano Newtons, as measured from the cantilever static deflection) and the contact duration (typically 100 ms for tip-substrate distance sweeps with 1s period). Charging times given here after (typically 1–4 min) always refer to the total duration of the approach-retract sweeps, whereas, the cumulated duration of the permanent contacts between the EFM tip and the CNT during the approach-retract sweeps, therefore corresponds to approximately one tenth of the charging process duration.

The global procedure for charge injection and detection is described in Fig. 4.11. First, EFM and topography images are acquired in an interleave scheme, such as described in Sect. 4.2.1, with the tip biased at a detection voltage V_{EFM} and lifted at a distance z above the substrate during the EFM pass. Then, a charge Q is injected in the nanotube using a tip voltage V_{inj} during the charge injection procedure. Finally, EFM data are acquired again after charge injection, with the tip bias set at V_{EFM}.

4.4.2 Experimental Illustration of EFM Signals

First of all, we present charging experiments [25] performed on a 19 nm diameter MWCNT (topography image in Fig. 4.12a) deposited on a 200-nm-thick $\mathrm{SiO_2}$ layer grown on a doped silicon substrate. The EFM image acquired with $V_{\mathrm{EFM}} = -3\,\mathrm{V}$ before charge injection is shown in Fig. 4.12b that reveals a dark footprint of the nanotube. The EFM signal is here the cantilever frequency shift Δf required to maintain a constant cantilever phase in the EFM pass (*see* Sect. 4.2.1). In absence of charge, the frequency shift Δf is due to the increase of the tip-substrate capacitance during the linear pass of the tip over the CNT. This capacitive signal is thus proportional to $(V_{\mathrm{EFM}} - V_{\mathrm{S}})^2$ (V_{S} being here negligible) and corresponds to a negative frequency shift (dark feature associated with the nanotube in Fig. 4.12b), which physically corre-

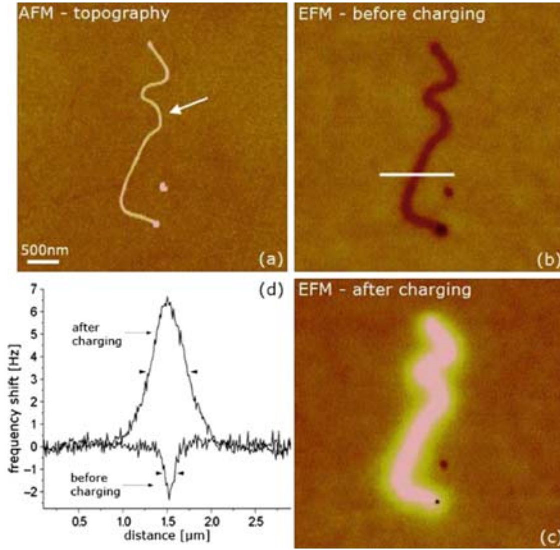

Fig. 4.12. (**a**) Atomic force microscopy image of MWCNT of $\sim 19\,\text{nm}$ diameter on a 200 nm silicon dioxide surface. (**b**) EFM image ($V_{\text{EFM}} = -3\,\text{V}$) acquired before charging (10-Hz color scale) with a tip-substrate distance $z \sim 100\,\text{nm}$. (**c**) EFM image taken in the same conditions, after a charge injection performed at the point indicated by an *arrow* in (**a**), using $V_{\text{inj}} = -5\,\text{V}$ for 2 min. (**d**) Cross-sections of the EFM scans for the case (**b**) and (**c**). The position of the cross-section is shown by the horizontal bar in (**b**). The full width at half minimum (FWHM) of the EFM signals before and the FWHM after charging (resp. $\sim$ 100 and 440 nm) is marked by the *triangles* as a guide to the eye. Adapted from [12]

sponds to a local increase of the attractive capacitive force on the cantilever when the tip is moved above the nanotube (*see* Fig. 4.1 in Sect. 4.2).

This behavior, however, no longer holds when the CNTs are charged because the total electric force also includes a component proportional to the nanotubes charge Q and to V_{EFM} (*see* Sect. 4.2). This is illustrated in Fig. 4.12c, showing the EFM signals after a charge injection experiment using $V_{\text{inj}} = -5\,\text{V}$ during 2 min at the injection point indicated by the *arrow* in Fig. 4.12a. The delocalization of the injected charge along the MWCNT is visible from the EFM image of Fig. 4.12c (taken after the injection), in which the nanotubes appear homogeneously bright. This contrast is due to $V_{\text{inj}} < 0$ (the nanotubes are negatively charged), and to the negative V_{EFM} values used for charge detection ($V_{\text{EFM}} = -3\,\text{V}$ in Fig. 4.12). The force component proportional to $\text{Q} \times V_{\text{EFM}}$ leads therefore to a positive frequency shift imaged as a bright feature in the EFM image (*see* Fig. 4.12c). It physically corresponds to the (here repulsive) interaction between the stored charge and capacitive charges at the EFM tip. An estimation based on numerical calculations gives here a nanotube linear charge density of $\sim 160|e|/\mu\text{m}$ [12, 30].

However, it should be mentioned that charge, capacitive and image charge force gradients compete altogether, so that even for $V_{\mathrm{EFM}} \times V_{\mathrm{inj}} > 0$, charged nanotubes can only be imaged as bright features provided charge signals predominate (1) over capacitive EFM signals proportional to $(V_{\mathrm{EFM}} - V_{\mathrm{S}})^2$ and (2) over the image charge contribution, which is proportional to Q^2 (*see* Sect. 4.2), which is enhanced when scanning on insulators. Such imaging conditions can be reached either for sufficiently charged CNTs or by lowering the detection bias V_{EFM}. These scanning conditions have been set for all EFM images presented in this section, so that dark and bright features will always correspond – unless explicitly stated – to capacitive and charge effects, respectively.

We now discuss the width of the cross-sections of EFM signals that are displayed in Fig. 4.12d, and have been taken at the CNT position indicated by the horizontal bar in Fig. 4.12b. The full width at half maximum (FWHM) of the EFM signal of the uncharged nanotubes equals ~ 100 nm, and is already larger than the apparent CNT diameter in the topography image, as can be seen from the AFM and EFM images in Fig. 4.12a, b, respectively. This point simply illustrates the lower spatial resolution of EFM compared with topography measurements, which is due to long-range electrostatic forces and the large (80–100 nm) tip-surface distance during EFM data acquisition. A more striking feature is the broadening of the EFM signals when the nanotube is charged (440 nm FWHM), as seen from Fig. 4.12d and from the comparison between Fig. 4.12b, c. This effect does not occur in EFM experiments performed in nanostructures deposited on conductors [13], where the width of EFM signals remains unchanged after charging. These two situations can be explained by the difference in the electrostatic screening induced by the substrate supporting the nanostructures [*see* [12, 25] for more details]. This change of FWHM for the charged nanotube is in practice a demonstration that the charge carried by the nanotube prior to the charging experiment is negligible, in contrast, for instance, with the case of DNA ropes deposited on similar substrates [24].

Finally, the delocalization of the injected charge has been found to exceed a few tens of microns along the CNTs [12,26], using charge injection experiments on carbon nanotube networks (*see* Fig. 4.13). The EFM image of the $\sim 40\,\mu$m as-grown nanotube network is presented in Fig. 4.13a (EFM image), showing the dark capacitive footprint of uncharged nanotubes. The black arrow indicates the injection point, and the injected charge is found to be delocalized along the whole network, as visible in Fig. 4.13b recorded after charge injection.

Abrupt Discharging Processes in Carbon Nanotubes

This section focuses on the phenomena associated with discharge processes in carbon nanotubes. First, we discuss abrupt discharging at single or multiple points along the CNT and at the CNT caps [25], which unambiguously demonstrate charge storage *in* carbon nanotubes. Next, we discuss the field emission

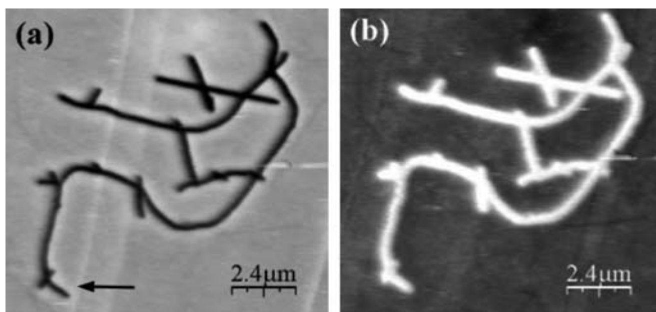

Fig. 4.13. (**a**) EFM image (frequency shift) of long SWCNTs network, performed before charge injection. The *black arrow* indicates the injection point. The dark nanotubes footprint corresponds to the uncharged network. (**b**) EFM scan after charging. The bright feature corresponds to a nearly uniform delocalized charge injected from one of the network extremity. Adapted from [26]

of charges to the oxide layer supporting the CNTs, and its enhancement at the CNT caps.

A sudden discharge behavior of the charge injected in a MWCNT with $\sim 18\,\text{nm}$ diameter and $\sim 2.3\,\mu\text{m}$ [12, 27] is presented in Fig 4.14. The point used for charge injection experiments is indicated by the arrow in the topography image (Fig. 4.14a). The EFM signal before charging (Fig. 4.14b) shows a negative frequency shift equal to 1.2 Hz. After the injection ($V_{\text{inj}} = -6$ during 3 min), the EFM scan is started from the bottom to the top (Fig. 4.14c). The nanotube appears first as homogeneously charged (bright feature with maximum frequency shift +8.2 Hz), but then undergoes three abrupt discharges at the points labeled d1, d2, and d3, each discharge occurring within one scan line. The CNT EFM image was then found stable on further scanning (no more sudden discharges), indicating that the bright halo surrounding the CNT capacitive footprint after the third discharge in Fig. 4.14c is due to charge emitted by the CNT and trapped in the oxide surface [25]. This effect will be discussed in the following section. The CNT frequency shifts before and after d1 are compared in Fig. 4.14d, and show that the capacitive footprint of the CNT topography can be already clearly identified after the first discharge, whereas the EFM signal was dominated by the CNT charge just after injection.

To associate the discharge locations at specific nanotubes points, an injection experiment has been made again at the same nanotube point using $V_{\text{inj}} = -7\,\text{V}$. The resulting EFM image scanned from top to bottom is shown in Fig. 4.14e, and was acquired $\sim 2\,\text{h}$ after the scan in Fig. 4.14c. Two abrupt discharges are evidenced in Fig. 4.14e, and correspond to the discharge points labeled d3 and d2 in Fig. 4.14c. This demonstrates that abrupt discharges are induced by specific points (likely due to the defects) along the MWCNT. At the discharge points, the CNT charge is field-emitted back to the EFM tip

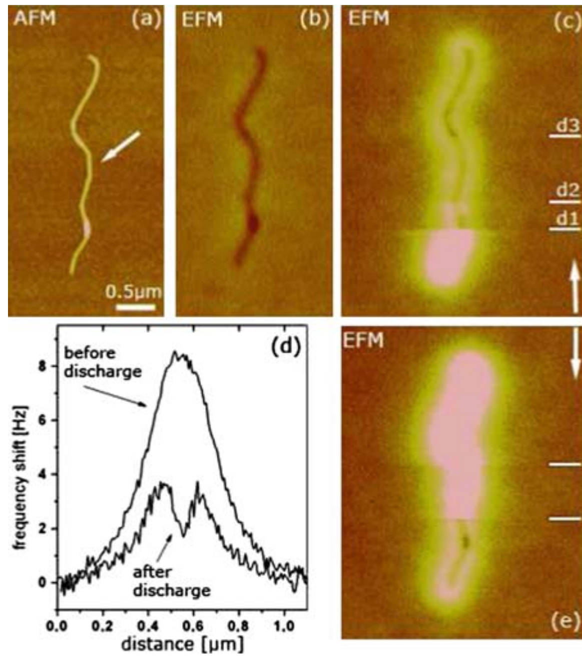

Fig. 4.14. (**a**) AFM topography picture of ∼ 2.3-µm-long MWCNT with ∼ 18 nm diameter. (**b**) EFM image acquired before charging. The capacitive footprint of the nanotube topography is visible and corresponds to a 1.2 Hz negative frequency shift. (**c**) EFM scan after charge injection with the tip biased at $V_{\mathrm{inj}} = -6\,\mathrm{V}$ for 3 min at the injection point marked in (**a**). The direction of data acquisition is indicated by the *vertical arrow*. Three discharge points (d1, d2, and d3 labeled in the figure) successively occur during the CNT scanning. After the discharge, the CNT capacitive footprint is clearly visible in the EFM image, however, surrounded by a bright halo. This EFM image proved stable on further scanning (no observable discharge). (**d**) EFM signal taken across the CNT before and after the sudden discharge labeled d1 in (**c**). (**e**) EFM scan after injection with the tip biased at $V_{\mathrm{inj}} = -7\,\mathrm{V}$. The image is scanned from top to the bottom (*see vertical arrow*). The two abrupt frequency shift drops that are visible in this scan correspond to the position of the discharges labeled d3 and d2 in (**c**). Adapted from [12]

apex that is grounded and intermittently brought into contact with the CNTs during the topography pass.

Charge Emission to the Oxide

The EFM images of Fig. 4.14c, e (after discharge) also display a residual negative charge along the nanotubes in the form of a bright halo around the nanotubes. The actual issue is to determine whether this negative charge corresponds to electrons still stored *in* the CNT, or to charge emitted by the CNT

and trapped on the oxide surface. If not discussed, the issue of surface charge emission can lead to potential misinterpretations of EFM images [12, 26–28]. In Fig. 4.14c, e, the bright halos observed after charging can be unambiguously attributed to charges trapped on the oxide surface for the following two reasons: (1) the residual charge pattern cannot be removed by discharging the nanotubes (i.e., performing a charge injection experiment on the CNT using $V_{\mathrm{inj}} = 0\,\mathrm{V}$) and (2) the residual charge pattern decays very slowly with time (order of a few hours), so that no evolution can be observed in the first subsequent EFM images acquired after the abrupt discharge phenomena. This behavior strongly contrasts with that of charge injected *in* the CNTs, which can be either removed by a local charge injection using $V_{\mathrm{inj}} = 0\,\mathrm{V}$ or abruptly emitted back to the EFM tip as described in the previous section. Moreover, the decay times of oxide charges stored in the vicinity of the nanotubes, which are found to be much longer than decay times on the bare oxide ($\sim 40\,\mathrm{min}$, *see* [12, 27]). The decay of charge injected in bare thin oxide layers has been proposed to result from the attraction between the oxide charge and their substrate images [29], leading to a gradual move of oxide charges toward the conductive substrate electrode. Here, the oxide charge near the CNTs is also subjected to an attractive image force from the CNTs themselves. This attractive interaction is consistent with the much longer retention times observed for oxide charge along the CNTs [25].

Continuous Discharge Processes

Interestingly, SWCNTs do not exhibit the abrupt discharging phenomena as in the case of the nanotube with bigger diameter [12, 27]. Here we discuss the fast continuous discharging of SWCNTs giving as an example the 1 nm diameter nanotube shown in Fig. 4.15a. The EFM scan taken before injection is shown in Fig. 4.15b. The nanotubes and metal markers appear here as dark features, corresponding to uncharged objects. The EFM scan after injection is displayed in Fig. 4.15c and shows the delocalization of the injected charge along the whole SWCNT length ($\sim 30\,\mu\mathrm{m}$), whereas the square metal markers remain uncharged. Clearly, no abrupt discharge occurs in Fig. 4.15c, while the CNT has been continuously scanned as shown in Fig. 4.15d and e, respectively, the time between two successive EFM images being $\sim 40\,\mathrm{min}$. A discharge – though not abrupt here – is evidenced by comparison of the SWCNT EFM images of Fig. 4.15c, d, whereas no significant change is observed on further scanning, as seen by comparison of Fig. 4.15d, e, and from the following EFM scans (not shown here). It is thus reasonable to conclude that the SWCNT in Fig. 4.15 undergoes a continuous discharge process.

Similar continuous discharging processes can be observed for MWCNTs, but, in contrast to SWCNTs, the discharge process shows a much longer timescale. An example is presented in Fig. 4.16. An $\sim$ 30-nm-diameter MWCNT shows only a weak decay of the total charge signal 13 h after charge injection (*see* Fig. 4.16a, b). In this case, a blurring of the MWCNT charge

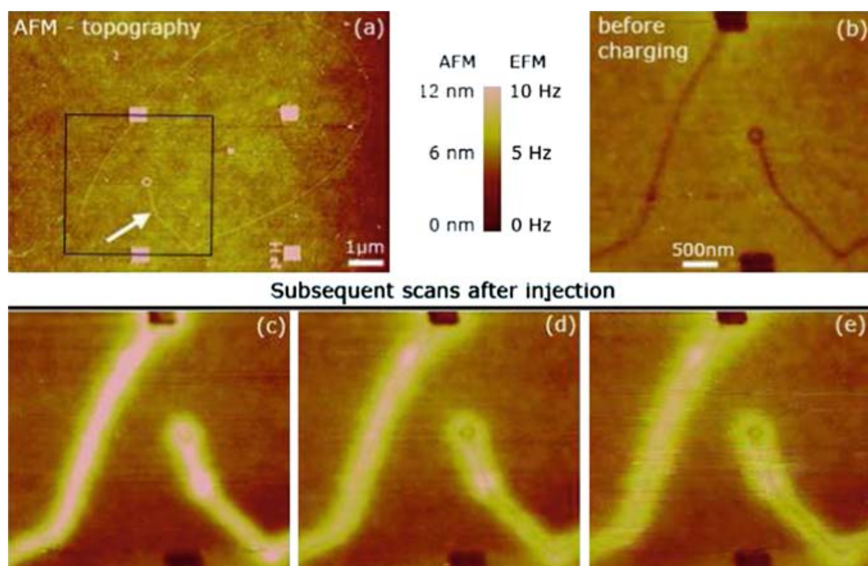

Fig. 4.15. (**a**) AFM topography image of a SWCNT with 1 nm diameter. $500 \times 500\,\text{nm}^2$ metal squares separated by a 5 μm pitch are visible in the image. One of the caps of the SWCNT appears to be ring-shaped. The length of the nanotubes is $\sim 32\,\mu\text{m}$. The arrow indicates the point used for charge injection experiments. (**b**) EFM image of the area indicated by the *black square* in (**a**), acquired before injection ($V_{\text{EFM}} = -3\,\text{V}$). (Inset) Color scale bars for the AFM topography and the EFM scans. (**c**) EFM image after a charge injection experiment with $V_{\text{inj}} = -5\,\text{V}$ for 3 min. The delocalization of the charge along whole nanotubes is visible. A *bright spot* can also be seen at the injection point, showing that charges were also injected locally into the dielectric surface. (**d**, **e**) Successive EFM scans acquired after the injection shown in (c). The SWCNT discharge is visible by comparison of (**c**) with (or to) (**d**), while no further discharge is observable afterward, as seen by comparison of (**d**) to (**e**). Adapted from [12]

signal can be observed in Fig. 4.16b. This is seen more clearly on the frequency shift cross-section in Fig. 4.16c, also showing the resurgence of the MWCNT capacitive frequency shift dip associated with the larger FWHM of the EFM signal 13 h after charge injection. Since the total EFM signal is approximately unchanged between Fig. 4.16a, b, it is assumed that the observed blurring of the EFM image corresponds to a slow emission of the MWCNT charge to the oxide, suggesting that the injected charges has been here stored in the nanotube for hours.

Nanotube Charge Versus Oxide Charge

Here, we illustrate the need for correct interpretations of EFM signals to demonstrate charge storage in SWCNTs and MWCNTs with respect to charge

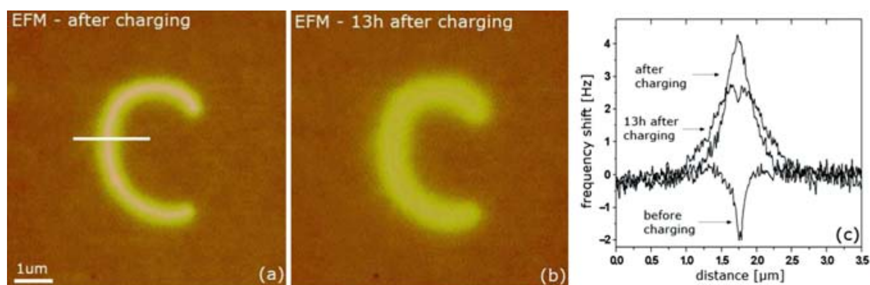

Fig. 4.16. (**a**) EFM image of a multiwalled carbon nanotube with 30 nm diameter just after charge injection. The horizontal bar across the nanotube indicates the place where the frequency shift cross-section has been taken. (**b**) EFM scan of the same nanotube 13 h after the charge injection. (**c**) Corresponding frequency shift cross-sections, together with the data acquired prior to charging. Adapted from [12]

storage in the oxide layer along the CNTs. While demonstrating the charging of a nanotube is relatively easy in the case of MWCNTs exhibiting abrupt discharging processes, it, however, needs to be assessed carefully in the case of SWCNTs, where the oxide charge can predominate over the CNT charge. To show this, comparative charge injection and EFM experiments performed on MWCNTs and SWCNTs need to be discussed. This is done in Fig. 4.17, showing the EFM data of a MWCNT (also used in Fig. 4.14) and a SWCNT ($\sim$ 3 nm diameter) acquired in the linear mode using $V_{\mathrm{EFM}} = -3\,\mathrm{V}$ and lift heights $z = 80$ and 60 nm, respectively. The negative EFM frequency shifts observed in Fig. 4.17a, c prior to charging experiments are the capacitive footprints of the nanotubes topography. After charging (with $V_{\mathrm{inj}} = -6\,\mathrm{V}$ for 2 min), the EFM signal of the MWCNT exhibits a pronounced positive frequency shift (*see* Fig. 4.17a), predominating over the capacitive signal and corresponding to a negative stored charge. A first evidence for charge storage in the MWCNT is given by the occurrence of an abrupt discharge while scanning, as discussed previously. Similar experiments have been performed on the SWCNT. Immediately after charging, the nanotubes height rises to 4.8 nm, and falls to 3.5 nm within the first EFM scan indicating that the SWCNT also undergoes a discharge, though not abrupt. The discharge is further evidenced by comparison of the EFM data of the two consecutive scans acquired after charging, showing the resurgence of the SWCNT capacitive frequency dip after the discharge (*see* Fig. 4.17c). These features show that some charge has indeed been injected in the SWCNT, but in contrast with the MWCNT, it only represents here a small fraction of the trapped oxide charge visible after the discharge, as seen from Fig. 4.17c,d. The issue of oxide charging thus needs to be taken in consideration in order to investigate the electrostatics of CNTs from EFM and charge injection experiments.

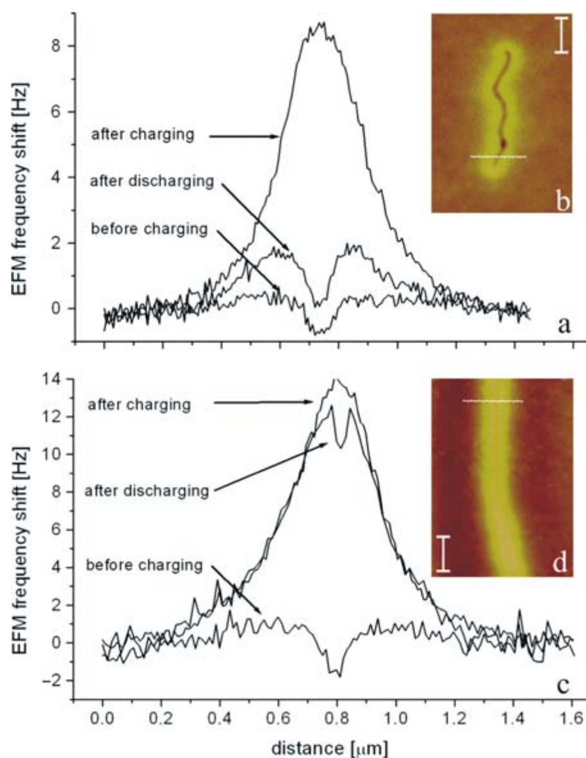

Fig. 4.17. (**a**) EFM frequency shifts ($V_{\mathrm{EFM}} = -3\,\mathrm{V}$) acquired across a 15 nm multiwalled carbon nanotube (*see horizontal line* in (**b**) before charging, after charging ($V_{\mathrm{inj}} = -6\,\mathrm{V}$ for 2 min), and after the MWCNT discharge. (**b**) EFM image (10 Hz scale) of the discharged MWCNT. The scale bar is 500 nm. (**c**) Similar EFM signals acquired on a 3.0 nm SWCNT. (**d**) EFM image (20 Hz scale) of the discharged SWCNT. The scale bar is 300 nm. Adapted from [13]

4.4.3 Inner-Shell Charging of CNTs

The detailed charge storage mechanisms of SWCNTs and MWCNTs and their relation with classical electrostatics – that is, do CNTs charge as capacitors? – have been established from EFM experiments [30], but require a truly quantitative analysis of the CNT charge states from EFM experiments. In this section, we discuss whether nanotubes behave like cylindrical metal capacitors – and thus only exhibit an outer-shell charging following a classical cylinder-plane capacitance, or whether they exhibit an internal response to the biased tip probe, allowing an inner-shell charging of the nanotubes. In order to find an answer to this question, one needs to keep in mind that on local charging of CNTs, there are three distinct behaviors: either the injected charge is mostly stored *in* the CNT, or mostly emitted by the CNT to the

substrate and trapped in the insulating SiO_2 layer, or finally stored both in the CNT and oxide traps.

The crucial issue to understand the electrostatics of CNTs from charge injection and EFM measurements is to perform a quantitative analysis of injected charge densities from EFM signals. Models derived from plane capacitor geometries have been used in early work on SWCNTs [26] but in order to get truly quantitative charge measurements, the EFM data are analyzed by comparing the CNT capacitive frequency shift Δf_c with the additional frequency shift Δf_λ observed after charging the CNT with a linear charge density λ, and compute the ratio $R = \Delta f_\lambda / \Delta f_c$ [31]. The quantities Δf_c and Δf_λ are in practice measured from the EFM images recorded prior to charging and after charge injection (*see*, e.g., Fig. 4.12). The advantage of this normalization procedure is that the ratio R does not depend on the spring constant of the cantilever, which enables direct comparisons between charging experiments on different CNTs. It gives the possibility to derive the linear charge densities (λ) of CNTs [30]. The relation of R and linear charge densities can be performed without any adjustable parameter from the z-component of electrostatic force gradients at the EFM tip and the ratio R between charge and capacitive frequency shifts.

The linear charge densities corresponding to experimental EFM data are presented in Fig. 4.18. EFM experiments have been performed on 25 nanotubes: 18 MWCNTs (*full symbols*) and 7 SWCNTs (*open symbols*). Linear charge densities have then been normalized by V_{inj}, and finally, plotted as a function of the CNT diameter d_{CNT}. For each CNT, it has been determined whether the charge was detected in the CNT (*squares*), trapped on the SiO_2 surface (*circles*), or in part in the CNT and in oxide traps (*diamonds*). For the purpose of comparison, classical electrostatic predictions for metal cylinders are also shown in Fig. 4.18 (*top curves*). The curve (a) corresponds to a cylinder-plane capacitance model, in a medium with an average dielectric constant accounting for the geometry of the CNT deposited on the oxide layer. Points shown in (b) have been obtained directly from the three-dimensional Poisson calculation with the EFM tip in contact with CNTs as in Fig. 4.11b.

One striking conclusion can be already drawn from Fig. 4.18: the experimental linear charge densities are found to deviate from classical electrostatic (curves a and b) predictions by more than one order of magnitude, already showing that CNTs (either MWCNTs or SWCNTs) *do not* charge like cylindrical capacitors. Within experimental accuracy, the experimental charge densities also exhibit a common variation law as a function of the CNT diameter d_{CNT}, irrespective of the actual charge location, that is mostly injected in the CNTs, in the oxide surface, or in part in CNTs and in oxide traps.

The reason for this effect is evidenced in Fig. 4.19, showing an energy diagram from the nanotube with the EFM biased at V_{inj} in contact with the nanotube, but prior to charge transfer to the nanotube or surface. Because of the finite transverse polarizability of the nanotube, the electric field generated at the EFM tip apex is seen to penetrate the MWCNT shells (Fig. 4.19,

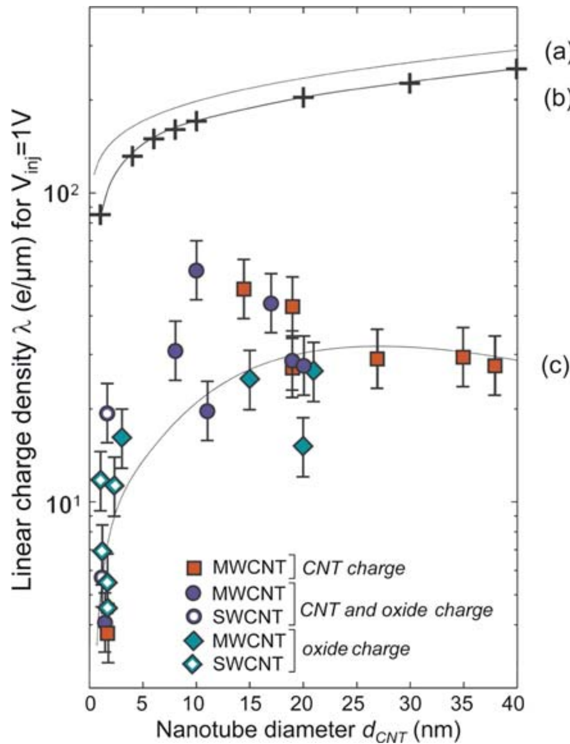

Fig. 4.18. Plot of the CNT linear charge density (in e/μm) as a function of the CNT diameter d_{CNT} for an injection voltage $V_{\mathrm{inj}} = 1\,\mathrm{V}$. The *top curves* correspond to densities expected for metal cylinders. The *curve* (**a**) is derived from the cylinder-plane capacitance. *Points* in (**b**) are obtained from three-dimensional Poisson calculations with the EFM tip in contact with the CNT as in Fig. 4.1a. The *line* in (**b**) is a guide to the eye. *Curve* (**c**) corresponds to linear charge densities expected from the inner-shell charging of nanotubes, as a response to the electric field generated by the EFM tip. Adapted from [30]

left), leading to a voltage drop across the MWCNT prior to charging. The charging of the MWCNT will then correspond to an equilibrium situation that takes place when the electrostatic energy of a nanotube will equal ΔV. Since $\Delta V < V_{\mathrm{inj}}$, this accounts for the fact that the experimental linear charge densities in Fig. 4.18 are found below the capacitive charging expectations. This process also accounts quantitatively for experimental observations (*see* line c in Fig. 4.18). The MWCNT inner-shell charging is finally explained by the fact that electrons are stored in the nanotube outermost (but possibly subsurface) metallic shell, in agreement with qualitative observations of charge storing in MWNCTs as seen from the abrupt discharging mechanisms shown in Fig. 4.14.

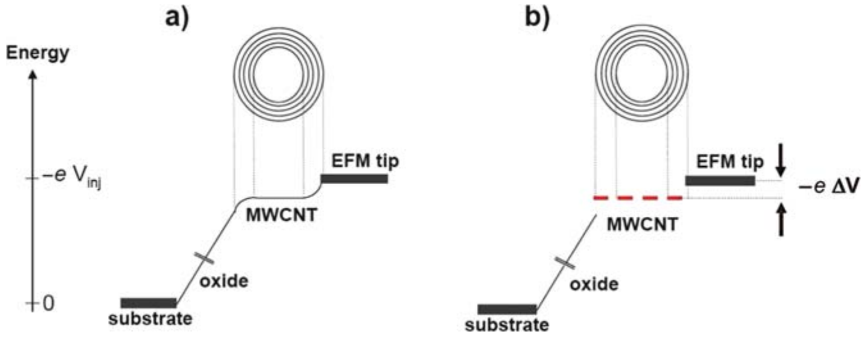

Fig. 4.19. *Left*: Schematics of the potential energy drop across the EFM tip/nanotube/oxide during the charge injection process (no charge transferred to the nanotube). *Right*: average of the potential energy for each shell, showing the voltage drop to be compensated by the nanotube charging is $\Delta V < V_{\text{inj}}$.

4.4.4 Electrostatic Interactions in SWCNTs

The above examples show that the EFM technique is useful to study the static distribution of electric charges in carbon nanotubes. It is interesting to point out that the theoretical calculation of charge distribution on SWCNTs had predicted U-like shapes of the charge distribution [32], with a charge accumulation at the tube ends stemming from Coulomb repulsion. These predictions, however, have been proposed for short CNTs ($< 100\,\text{nm}$). The EFM technique has been applied to verify if these theoretical findings are suitable, however, for longer CNTs.

Wang et al. [33] proposed study of the charge enhancement localized at the tube ends and simultaneously uniform charge density along the tube taking into account the oxide surface on which nanotube is deposited. They demonstrated that the previously predicted U-shape charge distribution in CNTs is present, but strongly weakened in conditions that are usually accessed by experiments (i.e., for tubes with μm length), in which a $\sim 20\%$ charge enhancement can be expected.

The linear charge distributions observed from EFM charging experiments of SWCNTs deposited on a SiO_2 substrate is shown in Fig. 4.20. In order to evidence the weak charge enhancement at the nanotube cap, a nonlinear color scale has been used in this figure. Note that the charge enhancement is localized only within 200 nm at the nanotube cap, and corresponds here [33] to the expected value for charge enhancement. This weak charge enhancement clearly shows that the charge distribution expected for short nanotubes is strongly modified for longer objects.

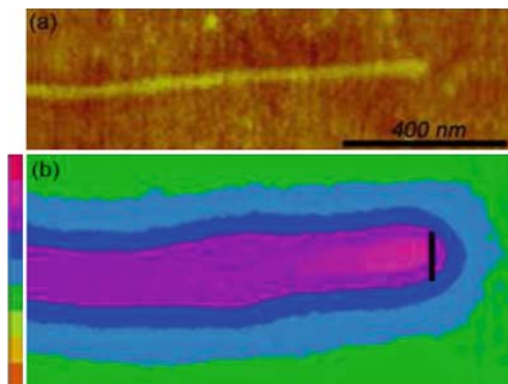

Fig. 4.20. (**a**) AFM topography image of single-walled nanotube with diameter 1.6 nm and length 2 µm deposited on SiO_2. (**b**) EFM scan of the same tube made after charge injection. A nonlinear color scale has been used in order to clearly show the weak enhancement at the tube end. The black line is a "guide to the eye" for the physical end of the tube. Adapted from [33]

4.5 Probing the Band Structure of Nanotubes on Insulators

Various measurements of the electronic properties of carbon nanotubes have been carried out at single molecular level since the discovery of nanotubes. Scanning tunneling spectroscopy has been mostly used for this purpose, providing for instance very valuable information about Van Hove singularities of the nanotube density of states [34]. In these experiments, nanotubes need to be deposited over a metallic substrate to allow electrons to tunnel to/from a scanning tunneling spectroscopy tip. However, because of the nanotube–substrate interaction, many of their properties could not be investigated. EFM techniques give the possibility to circumvent this problem allowing the characterization of the electronic properties of nanotube on insulators. The subject of this section is to give short overview on recent studies carried out *on insulators*, on the assessment of the metallic/semiconducting character and of the local density of states of SWCNTs.

4.5.1 Imaging the Semiconductor/Metal Character of Carbon Nanotubes

The electrostatic response of charged carbon nanotubes probed by EFM technique can be used to investigate the metallic/semiconducting character of the carbon nanotubes. Barboza et al. [35] have recently reported on a semiconductor–metal transition for SWCNTs monitored from EFM experiments.

Charging and EFM experiments used in this work were similar to technique described previously, except that no bias is applied between the tip and the

sample ($V_{EFM} = 0$) during the second pass of EFM imaging, so that the EFM signal consists solely in the image charge interactions (interaction with the nanotube charge together with their electrostatic image with respect to the metal-plated tip). This corresponds to the $(V_Q)^2$ term in (4.3), leading to an always negative frequency shift (force gradient associated with the attractive image charge interaction).

Semiconducting and metallic tubes used in the EFM experiments were first preselected by Raman spectroscopy studies in order to determine their semiconducting/metallic character and chirality. Then, each tube was subjected to charge injection, and EFM data were recorded as a function of tip injecting bias (V_{inj}), using a minimal and constant ($\sim 0.3\,\mathrm{N/m}$) tip-nanotube force during the injection process.

Barboza et al. measured the linear charge densities as a function of V_{inj} for metallic and semiconducting nanotubes (*see* Fig. 4.21). For a metallic nanotube, the charge-bias plot (black squares) exhibits a nicely linear symmetric behavior with a minimum bias of approximately $\pm 2\,\mathrm{V}$ necessary for detection of extra charge at the nanotube. The charge-bias plot for semiconducting nanotubes (in red) exhibits an important difference compared with the metallic tube: the plot is asymmetrical with respect to the injection bias (*see* the deviation at $V_{inj} = -3\,\mathrm{V}$), and the charge density is also smaller than that for metallic tubes for a given V_{inj}.

In the second part of the charging experiment, the injection bias (V_{inj}) and injection time were kept constant. The linear charge densities were measured as a function of the compressive tip-tube force (per unit length) during the injection (*see* Fig. 4.21b). For the metallic tube (dark squares), charge densities exhibit a rather weak dependence on the compressive force. Semiconducting nanotubes, however, show striking features on the increase of

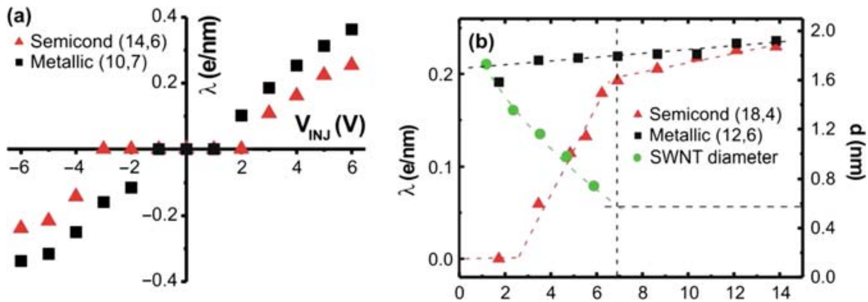

Fig. 4.21. (**a**) Plot of the charge density (λ) versus injection bias (V_{inj}) for metallic (*black squares*) and semiconducting tube (*red triangles*). (**b**) Plot of the charge density (λ) as a function of the force (per unit of length) applied during nanotube charging for metallic and semiconducting tube, *black squares* and *red triangles*, respectively. The evolution of the semiconducting nanotube as the compressive force is applied is represented by green circles. The dashed lines are guides for the eye. Adapted from [35]

the compressive force. For a small EFM tip force during the charge injection, no injected charge is detected whereas for bigger force ($> 3\,\mathrm{N/m}$), a steep increase of charge density is detected until it reaches the value measured for metallic tube. This effect was attributed by Barboza et al. to a semiconducting-to-metal transition on an applied external compressive force.

4.5.2 Imaging the Density of States of Carbon Nanotubes

Probing of local density of states in carbon nanotubes is certainly another remarkable capability of the EFM technique. In order to show this, Heo et al. [36] proposed an experiment that is carried out in a similar way as described earlier. However, the slow scan axis is disabled, so the tip always scans the same line across the sample. A nanotube lying on the oxide layer is scanned in two modes: standard tapping mode (topography) and EFM mode. In the latter one, the tip is set at very low tip-sample height (typically a few nanometers). During each second pass (EFM mode), the tip is biased at voltage V_{EFM} and phase shift ($\Delta\varphi$) between the mechanical drive and the cantilever motion is recorded.

The biased EFM tip (V_{EFM}) is used to vary the Fermi level tube (by changing V_{EFM}). The local density of states drastically increases whenever the Fermi level is swept through a van Hove singularity in the density of states. This changes the cantilever-tube coupling, and thus the mechanical oscillation of the tip, which is detected during the experiment and V_{EFM} sweep. The upper panel of Fig. 4.22 shows a color scale plot of the cantilever phase shift $\Delta\varphi$ versus ΔV and tip position Δx along a 0.9 nm diameter SWCNT. $\mathit{\Delta V}$ is here proportional to V_{EFM} (*see* [36] for more details). The dashed line indicates the nanotube position. The lower panel of Fig. 4.22 shows the plot of $\Delta\varphi$ versus ΔV when the tip is directly over the nanotube. The plot follows the trend $\Delta\varphi \sim -\Delta V^2$; however, some kinks are seen for certain voltages (indicated by the *arrows*), which are clearly visible in the when the data background is subtracted (Fig. 4.22b): now the plot follows approximately the trend $-d^2(\Delta\varphi)/\Delta V^2$ and it shows series of peaks as ΔV varies. These peaks occur at the same voltage position of the kinks presented in Fig. 4.22a. According to [36] the peaks in the $\mathit{\Delta\varphi}$ directly reflect the one-dimensional van Hove singularities of the tube. The voltage position of the peaks is nanotube dependent, as expected for tubes with different electronic structure and thus allowing distinguishing between individual metallic and semiconducting tubes.

The possibility to measure the dielectric polarization of individual SWCNTs has also been proposed recently by [37]. According to them, the longitudinal dielectric constants (probed by EFM) can exhibit different responses for metallic and semiconducting tubes, thus allowing the assessment of the electronic character of the nanotubes (*see* [37] for more details).

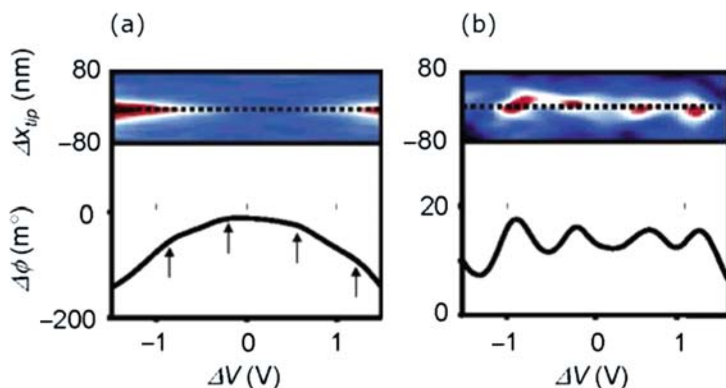

Fig. 4.22. (**a**) *Upper panel*: color plot of the phase shift ($\Delta\varphi$) as a function of tip position (Δx) and voltage ΔV, where ΔV is proportional to V_{EFM} (*see* Heo et al. (2005) for more details). The dotted line shows the position of the tube. *Dark red* corresponds to $-150\,\mathrm{m}^{\circ}$ whereas *dark blue* corresponds to $0.0\,\mathrm{m}^{\circ}$. *Lower panel*: $\Delta\varphi$ versus ΔV when the tip is directly above the tube (*dotted line* in *upper panel*). *Arrows* indicate the kinks in the plot. (**b**) *Upper panel*: color plot of $\Delta\varphi$ versus Δx and voltage ΔV when the background is subtracted taken. *Dark red* corresponds to $20\,\mathrm{m}^{\circ}$ whereas *dark blue* corresponds to $5\,\mathrm{m}^{\circ}$. *Lower panel*: $\Delta\varphi$ versus ΔV taken along the *dotted line* exhibiting a series of peaks. The voltages giving the peaks correspond to the voltages yielding the kinks in the data in the lower panel of (**a**). Adapted from [36]

4.6 KFM Studies of Nanotube Devices

This section describes the use of electrical techniques derived from AFM to probe the electrostatic properties of carbon nanotube devices such as CNT-FETs. To map, for example, voltage drops along nanotubes, KFM-based studies (or surface potential measurements) are here preferred to EFM studies (i.e., charge measurements), which were reviewed in the previous sections. Here we describe the work done using KFM techniques on carbon nanotube devices, starting from the study of charge transfers at the nanotube–contact interfaces, the assessment of diffusive/ballistic character of transport along SWCNTs, and finally, more recent studies performed on CNTFETs under operation.

4.6.1 Charge Transfers at Nanotube–Metal Interfaces

Field effect transistors based on carbon nanotubes with controlled or minimized Schottky barrier heights have been demonstrated by [38] using palladium electrodes. From an electrostatic point of view, the study of the formation of electrical contacts with ohmic or Schottky character between metals and nanotubes can be performed by studying the contact potential

difference (or charge transfer) between metals to nanotubes. This idea corresponds in fact to the first use of the Kelvin probe implementation in an AFM [10], in which the contact potential difference was measured between different metals (gold and palladium), with a sensitivity of a few tens of millivolt.

The idea followed by [39] was based on the fact that CNTFETs operate as p-type devices in air (i.e., Schottky barrier transistors with hole transport) ([2, 3]), even though not intentionally doped, whereas devices probed in ultrahigh vacuum (UHV) behave as n-type devices (i.e., Schottky barrier transistors with electron transport) [40,41]. This change of behavior has been investigated using KFM by dispersing SWCNTs[3] on a flame-annealed Au surface (*see* Fig. 4.23), and monitoring the associated contact potential difference by KFM (contrast in the surface potential image).

The nanotubes on Au in the KFM image of Fig. 4.23b, *taken in air*, appear as bright features (positive surface potential with respect to the surface), indicating a positive charging of the nanotube due to a lower vacuum level. The measured contact potential difference is approximately +60mV. This behavior is, however, opposite (*see* Fig. 4.23c) after a long stay of the sample in UHV, after which the nanotubes are seen as dark features in the KFM image

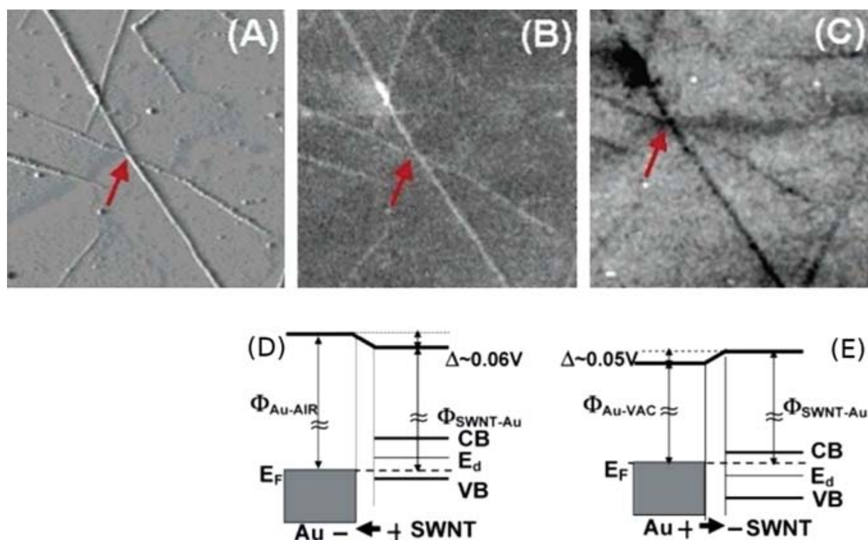

Fig. 4.23. (**a**) AFM topographic images of nanotubes deposited on a flame-annealed Au (111) surface. (**b**, **c**) KFM images obtained in air and after a long period in ultrahigh vacuum (*UHV*) (Au). The bright contrast indicates a lower vacuum level. (**d**, **e**) Energy diagrams showing the energy-level alignment between a SWCNT and Au in air and UHV, respectively. Adapted from [39]

[3] The contact potential difference of multiwalled carbon nanotubes have also been investigated by KFM: [18]

(negative nanotube charging) due to a higher vacuum level compared with Au, with here a negative contact potential difference of approximately −50mV. The two diagrams, corresponding to p-type (respectively n-type) carbon nanotubes are shown in Fig. 4.23d,e, and are found consistent with the p-type (respectively n-type) transport behavior of SWCNT FET devices in air or UHV [41].

In order to probe energy level alignments, similar experiments using KFM have been carried out more in the case of ferromagnetic contacts used for spintronic applications. Shiraishi et al. [42] measured the contact potential difference at the Ni–SWCNT and Co–SWCNT interfaces, and found them equal −52 and −27 mV, respectively. The corresponding energy-level alignment diagrams (*see* [42]) suggest that holes could be suitable spin carriers for SWCNT spin devices.

4.6.2 Diffusive and Ballistic Transport in Carbon Nanotubes

The transport properties of carbon nanotubes probed by KFM have been discussed in terms of diffusive and ballistic transport by [14] both for MWCNTs and SWCNTs. The authors used an ac-EFM technique, which is equivalent to an open-loop KFM technique (*see* Sect. 4.2 for details), the ac-bias being applied across the nanotube so as to reduce side capacitance effects [43]. Additionally, the ac-EFM signal is here subtracted from the background signal across the electrodes, so as to get rid of the stray capacitive coupling of the tip to the metal electrodes. ac-EFM maps can therefore be viewed as the local measurement of the attenuation of an ac voltage along carbon nanotubes.

ac-EFM measurements are presented in Fig. 4.24 for both an MWCNT and an SWCNT [14]. The ac-EFM signal of the MWCNT is presented in Fig. 4.24a,b, in which the nanotube left electrode is subjected to the ac bias of 150 mV. The KFM signal shows here a linear drop, indicating that the nanotube behaves as a diffusive conductor. The ac-EFM signal of a bundle of SWCNTs is then presented in Fig. 4.24c, and shows no measurable intrinsic resistance (plateau in the ac-EFM cross-section of Fig. 4.24d) when the ac-EFM signal is projected across the electrodes, which was – in conjunction with the nanotube transport properties – taken as a signature of the ballistic transport in the bundle of SWCNTs [14].

4.6.3 Kelvin Force Microscopy of CNTFETs

Backgate Operation of CNTFETs

We now turn to the characterization of CNTFETs using KFM techniques. A CNTFET based on a bundle of SWCNTs has been fabricated using Ti electrodes as source and drain contacts, a 300-nm-thick silicon dioxide layer as a gate dielectric and a p-doped silicon wafer as a backgate (*see* Fig. 4.25) [44, 45]. KFM images (here, in vacuum, using an FM-KFM method as described

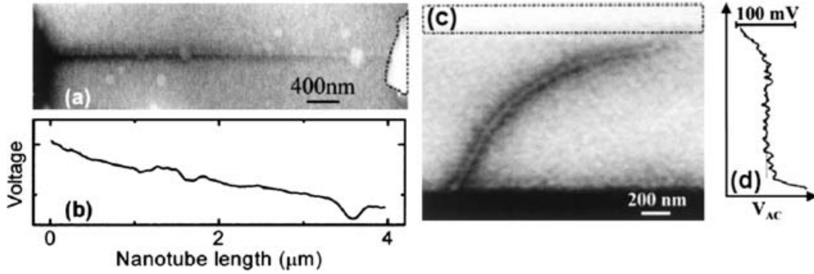

Fig. 4.24. (**a**) ac-Electrostatic force microscopy (*ac-EFM*) image of a multiwalled carbon nanotube of diameter 9 nm. An ac-bias of 150 mV is applied to the left electrode. (**b**) ac-EFM signal as a function of the MWCNT length. (**c**) ac-EFM image of a metallic bundle of SWCNTs with diameter 2.5 nm. An ac bias of 100 mV is applied to the lower electrode. (**d**) The ac-EFM signal exhibits a plateau along the length of the SWCNT bundle. Adapted from [14]

in Sect. 4.4) have been obtained for various source-drain voltages and various gate potentials. Examples are provided in Figs. 4.25a, b for $V_{DS} = 1$ and 3 V respectively, both at $V_{GS} = 3$ V. KFM profiles are then plotted for various values of gate voltage ranging from $V_{GS} = -2$ to 2 V at $V_{DS} = 1$ V (*see* Fig. 4.25b) and $V_{DS} = 3$ V (*see* Fig. 4.25d). In these profiles, the potential drops along the nanotube are strongly influenced by applying a gate potential. The difference of potential at the drain edge is also strongly modulated, in agreement with Schottky barrier FET models for carbon nanotube transistors [46, 47].

KFM Determination of the lever arm of a CNTFET

The crucial issue to understand KFM experiments on transistors is to derive quantitative information from KFM images, even though the role of side capacitances has been pointed out earlier [15, 43]. We here present a KFM study performed on Pd-contacted CNTFETs fabricated on an ∼ 320 nm-thick SiO_2 layer, which addresses this issue [48]. It is shown in particular that the lever arm between the backgate bias and nanotube electrostatic potential shifts – of strong interest to characterize the CNTFET operation – can be assessed from such experiments.

The electrostatics of the CNTFET as seen from KFM experiments can be written using the side-capacitance approach introduced by [15]:

$$V_{KFM} = \alpha_{NT} V_{NT} + \alpha_G V_G + \alpha_D V_D + \alpha_S V_S \tag{4.7}$$

Here the KFM dc bias V_{KFM} is written as a weighted average of the nanotube electrostatic potential V_{NT}, of the backgate electrostatic potential V_G, and of the source and drain electrodes at voltages V_D and V_S, respectively. In (4.7), the coefficients α_i refer to the weighted average between capacitance

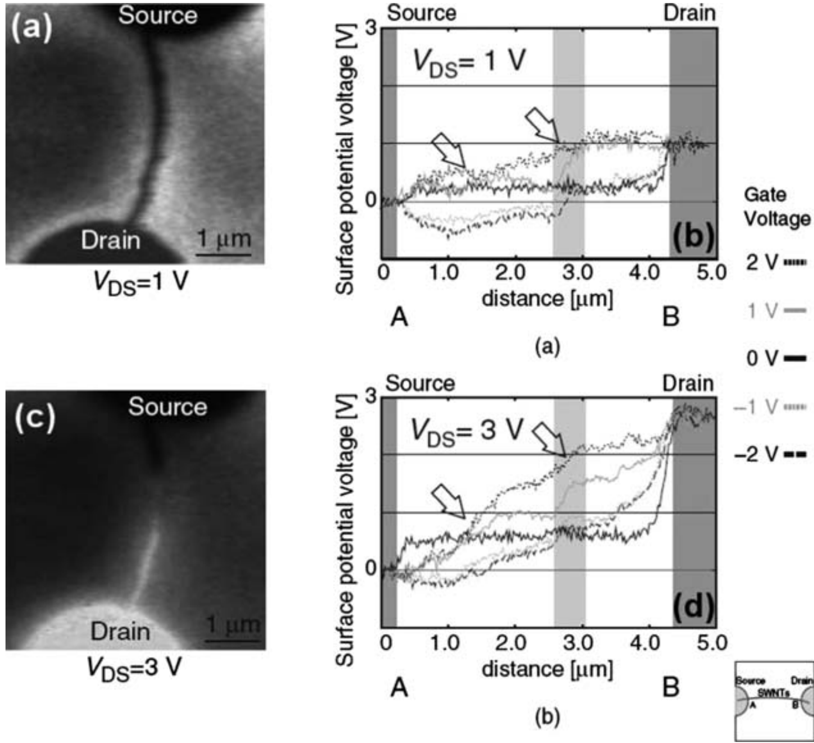

Fig. 4.25. (**a**) KFM image of a bundle of SWCNTs connected with Ti electrodes at $V_{\text{DS}} = 1\,\text{V}$ and $V_{\text{GS}} = 3\,\text{V}$. (**b**) Surface potential profiles at $V_{\text{DS}} = 1\,\text{V}$ for V_{GS} from -2 to $2\,\text{V}$. (**c**) KFM image of the same bundle of SWCNTs as at (**a**) $V_{\text{DS}} = 3\,\text{V}$ and $V_{\text{GS}} = 3\,\text{V}$. (**d**) Surface potential profiles at $V_{\text{DS}} = 3\,\text{V}$ for V_{GS} from $-2\,\text{V}$ to $2\,\text{V}$. In (**b**) and (**d**), the dark shaded areas correspond to the source and drain electrodes. Adapted from [44]

derivatives, as described in details in Sect. 4.4, which are here determined phenomenologically. Using $V_{\text{NT}} = \beta V_{\text{G}}$ (β being the electrostatic lever arm for the CNTFET), and $\alpha_{\text{NT}} + \alpha_{\text{G}} + \alpha_{\text{D}} + \alpha_{\text{S}} = 1$ for the sum of the weights in (4.7), this description requires the experimental determination of four independent coefficients.

This can be done by using the recorded KFM voltage drop across the device when the nanotube is subjected to a source-drain bias $V_{\text{DS}} = -3\text{V}$ (the source is grounded here). From the KFM bias recorded at the source, one obtains $\alpha_{\text{D}} \sim 1\%$ and from the voltage drop across the device (here $600 \pm 50\,\text{mV}$), one gets $\alpha_{\text{D}} + \alpha_{\text{NT}} = 20 \pm 2\%$, that is $\alpha_{\text{NT}} = 19 \pm 2\%$. To determine the two remaining relations and find all the α_i and β, one then uses the KFM maps of the operating device, recorded at different backgate bias V_{G} (*see* Fig. 4.26). Such maps give two information: (1) the slope of the variation of V_{KFM} as a function of V_{G} recorded *off the nanotube*, and which corresponds to $(\alpha_{\text{NT}} + \alpha_{\text{G}})$; and (2) the slope of the variation of V_{KFM} as

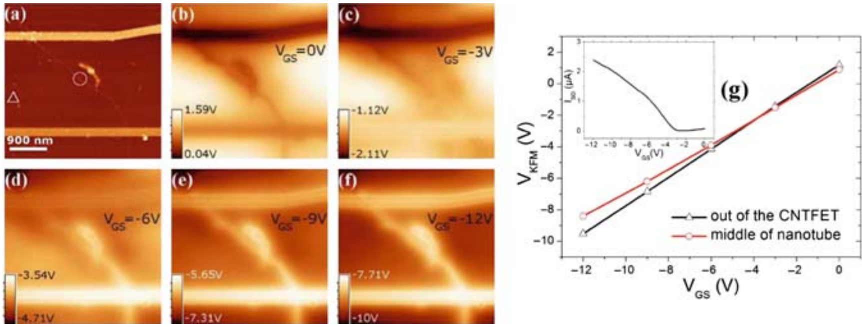

Fig. 4.26. (**a**) AFM image of a single-walled nanotube field effect transistor. Scale bar: 900 nm. (**b**–**f**) Associated KFM images at $V_{DS} = -3$ V, (**b**) $V_{GS} = 0$ V, (**c**) $V_{GS} = -3$ V, (**d**) $V_{GS} = -6$ V, (**e**) $V_{GS} = -9$ V, and (**f**) $V_{GS} = -12$ V. (**g**) Recorded KFM voltage on the nanotube (*circles*) and off the nanotube (*triangles*) as a function of the device gate bias V_G, in the range of operation of the CNTFET (*see* inset for the CNTFET transfer characteristics). Adapted from [48]

a function of V_G recorded with the tip above the nanotube, which provides a direct measurement of $(\alpha_{NT}\beta + \alpha_G)$. Data extracted from Fig. 4.26 give $\alpha_{NT} + \alpha_G = 0.89 \pm 0.02$, and $\alpha_{NT}\beta + \alpha_G = 0.75 \pm 0.02$. These values lead to the following determination of the α_i and β coefficients: $\alpha_{NT} = 19\pm2\%$, $\alpha_G = 70 \pm 2\%$, $\alpha_S = 10 \pm 2\%$ and $\beta = 0.26 \pm 0.15$. These figures show that with fairly large tip substrate distances (here $z \sim 80$ nm), the weight α_{NT} associated with the nanotube detection is quite weak. This is in fact strongly enhanced when operating in UHV, because the tip-substrate distance in noncontact AFM measurements is typically less than 20 nm, and thus will enhance the capacitive weight α_{NT} compared with α_G, α_S, and α_D. Also, the electrostatic lever arm of the nanotube has been here determined quantitatively, with a $\beta = 0.26\pm0.15$ value close to experimental values already reported in literature for CNTFET devices with similar geometries [49,50], and estimated from, for example, Coulomb blockade effects at low temperature.

Hysteretic Behavior of CNTFETs and Surface Charges

A similar study as in Sect. 4.6.3 has been performed with a 1.1 nm diameter SWCNT field effect transistor [51]. The authors were interested in the origins of the hysteresis of a CNTFET, associated with out-of-equilibrium charge storage in the CNTFET environment, and for which several possibilities have been proposed in literature: charging at the nanotube–ambient air interface [52], at the nanotube–SiO_2 interface [49,53], or at the Si$-$$SiO_2$ interface [49, 54].

Here, Umesaka et al. first applied a bias stress to the backgate of -5 V (and $+5$ V), and later recorded the KFM images of the device, shown respectively in Fig. 4.27a,b. KFM profiles have then been taken across the nanotube for

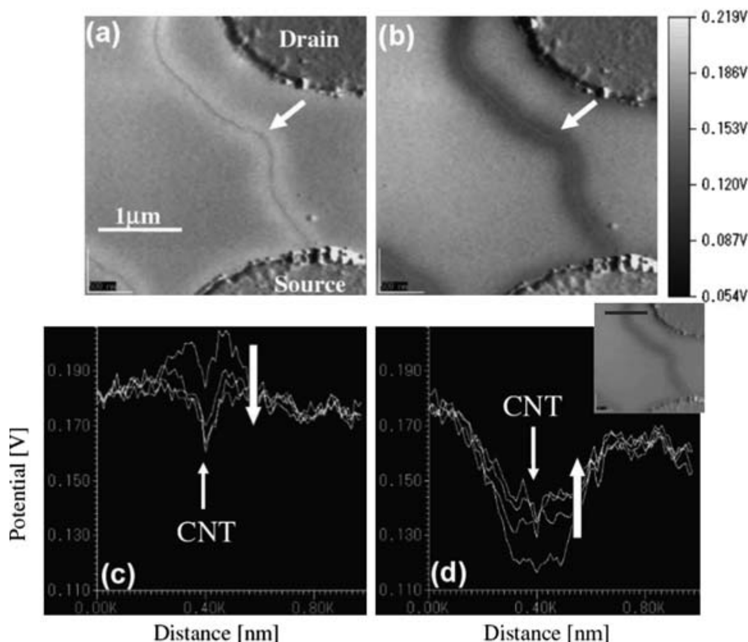

Fig. 4.27. *Top*: surface potential images of a CNTFET at $V_{GS} = 0\,V$ and $V_{DS} = -0.3\,V$ (**a**) just after applying $-5\,V$ gate bias stress and (**b**) just after applying $+5\,V$ gate bias stress. *Bottom*: Line profiles of the surface potential of the CNTFET at $V_{GS} = 0\,V$ taken 0, 15, 30, and 45 min after applying the gate bias stress. The graphs in (**c**) and (**d**) correspond respectively to a $-5\,V$ gate bias stress and a $+5\,V$ gate bias stress. The bar in the inset indicates the position of the line profiles. Adapted from [51]

different times after the gate stress. The results are shown in Fig. 4.27c and d, respectively, for the $-5\,V$ stress and the $+5\,V$ stress. The nanotube environment shows a positive (respectively negative) surface potential after the $-5\,V$ (respectively $+5\,V$) gate bias stress, both charging effects decaying with time. This indicates a capacitive response of the nanotube channel to the backgate with opposite charges trapped into the oxide layer surrounded the nanotube, in agreement with the hysteresis observed in the CNTFET operation [51].

4.7 Conclusion

In this chapter, we have reviewed recent experimental studies carried out on carbon nanotubes using electrical techniques derived from AFM. It has been shown, on the one hand, that the dielectric and charging properties of individual carbon nanotubes can be measured experimentally, using EFM, and revealing peculiar electrostatic properties associated with their

one-dimensional, semiconducting, or multishell properties. On the other hand, it has been demonstrated that KFM and related techniques are invaluable so as to bring insight into the operation of devices based on carbon nanotubes, including the formation of electrical contacts and of charge transfer at nanotube–metal interfaces, the assessment of diffusive or ballistic character of transport along SWCNTs, and quantitative measurements on CNTFETs, such as the electrostatic lever arm governing the transistor operation. Such studies, together with the ongoing and future developments of electronic characterization tools using nanoscale force measurements, especially in UHV environments and/or at low temperature, should bring a valuable insight for such fields of research combining nanoscience and nanotechnology.

Acknowledgement

The authors acknowledge fruitful discussions with L. Adamowicz, H. Diesinger, V. Derycke, D. Deresmes, A. Mayer, Z. Wang, and M. Devel.

References

1. S. Iijima, Nature **354**(6348) 56 (1991)
2. S.J. Tans, A.R.M. Verschueren, C. Dekker, Nature **393** 49 (1998)
3. R. Martel, T. Schmidt, H.R. Shea, T. Hertel, P. Avouris, Appl. Phys. Lett. **73** 2447 (1998)
4. G. Binnig, H. Rohrer, C. Gerber, E. Weibel, Phys. Rev. Lett. **49** 57 (1982)
5. G. Binnig, C.F. Quate, C. Gerber, Phys. Rev. Lett. **56** 930 (1986)
6. Y. Martin, D.W. Abraham, H.K. Wickramsinghe, Appl. Phys. Lett. **52** 1103 (1988)
7. J.E. Stern, B.D. Terris, H.J. Mamin, D. Rugar, Appl. Phys. Lett. **53** 2717 (1988)
8. B.D. Terris, J.E. Stern, D. Rugar, H.J. Mamin, Phys. Rev. Lett. **63** 2669 (1989)
9. C. Schönenberger, S.F. Alvarado, Phys. Rev. Lett. **65** 3162 (1990)
10. M.N. Nonnenmacher, M.P. O'Boyle, H.K. Wickramsinghe, Appl. Phys. Lett. **58** 2921 (1991)
11. T.D. Krauss, L.E. Brus, Phys. Rev. Lett. **83** 4840 (1999)
12. M. Zdrojek, T. Mélin, H. Diesinger, D. Stiévenard, W. Gebicki, L. Adamowicz, J. Appl. Phys. 100 **114326** (2006)
13. T. Mélin, H. Diesinger, D. Deresmes, D. Stiévenard, Phys. Rev. Lett. **92** 166101 (2004)
14. A. Bachtold, M.S. Fuhrer, S. Plyasunov, M. Forero, E.H. Anderson, A. Zettl, L. P. McEuen, Phys. Rev. Lett. **84** 26 (2000)
15. H.O. Jacobs, P. Leuchtmann, O.J. Homan, A. Stemmer, J. Appl. Phys. **84** 1168 (1998)
16. S.C. Chin, Y.C. Chang, C.C. Hsu, W.H. Lin, C.I. Wu, C.S. Chang, T.T. Tsong, W.Y. Woon, L.T. Lin, H.J. Tao, Nanotechnology **19** 325703 (2008)
17. S.B. Arnason, A.G. Rinzler, Q. Hudspeth, A.F. Hebard, Appl. Phys. Lett. **75** 2842 (1999)

18. C. Maeda, S. Kishimoto, T. Mizutani, T. Sugai, H. Shinohara, Jpn. J. Appl. Phys. **42** 2449 (2003)
19. M. Bockrath, N. Markovic, A. Shepard, M. Tinkham, L. Gurevich, L.P. Kouwenhoven, M.W. Wu, L.L. Sohn, Nano Lett. **2**(3) 187 (2002)
20. C. Staii, A.T. Johnson, J. Nicholas, Nano Lett. **4**(5) 859 (2004)
21. T.S. Jespersen, J. Nygård, Nano Lett. **5**(9) 1838 (2005)
22. N. Geblinger, A. Ismach, E. Joselevich, Nat. Nanotechnol. **3** 195 (2008)
23. T.S. Jespersen, J. Nygård, Appl. Phys. Lett. **90**, 183108 (2007)
24. T. Heim, T. Mélin, D. Deresmes, D. Vuillaume, Appl. Phys. Lett. **85** 2637 (2004)
25. M. Zdrojek, T. Mélin, B. Jouault, M. Wozniak, A. Huczko, W. Gebicki, D. Stiévenard L. Adamowicz, Appl. Phys. Lett. **86** 213114 (2005)
26. M. Paillet, P. Poncharal, A. Zahab, Phys. Rev. Lett. **94** 186801 (2005)
27. M. Zdrojek, T. Mélin, H. Diesinger, W. Gebicki, D. Stiévenard, L. Adamowicz, Phys. Rev. Lett. **96** 039703 (2006)
28. M. Paillet, P. Poncharal, A. Zahab, Phys. Rev. Lett. **96** 039704 (2006)
29. J. Lambert, G. Loubens, C. Guthmann, M. Saint-Jean, T. Mélin, Phys. Rev. B. **71** 155418 (2005)
30. M. Zdrojek, T. Heim, D. Brunel, A. Mayer, T. Mélin, Phys. Rev. **B 77** 033404 (2008)
31. T. Mélin, H. Diesinger, D. Deresmes, D. Stiévenard, Phys. Rev. B **69** 035321 (2004)
32. P. Keblinski, S.K. Nayak, P. Zapol, P.M. Ajayan, Phys. Rev. Lett. **89** 255503 (2002)
33. Z. Wang, M. Zdrojek, T. Mélin, M. Devel, Phys. Rev. B **78** 085425 (2008)
34. J.W.G. Wildoer, L.C. Venema, A.G. Rinzler, R.E. Smalley, C. Dekker, Nature **391** 59 (1998)
35. A.P.M. Barboza, A.P. Gomez, B.S. Archanjo, P.T. Araujo, A. Jorio, A.S. Ferlauto, M.S.C. Mazzoni, H. Chacham, B.R.A. Neves, Phys. Rev. Lett. **100** 256804 (2008)
36. J. Heo, M. Bockrath, Nano Lett. **5** 853 (2005)
37. W. Lu, Y. Xiong, A. Hassanien, W. Zhao, M. Zheng, L. Chen, Nano Lett. **9**, 1664 (2009)
38. A. Javey, J. Guo, Q. Wang, M. Lundstrom, H. Dai, Nature **424** 654 (2003)
39. X. Cui, M. Freitag, R. Martel, L. Brus, P.h. Avouris, Nano Lett. **3** 783 (2003)
40. V. Derycke, R. Martel, J. Appenzeller, P. Avouris, Nano Lett. **1** 453 (2001)
41. V. Derycke, R. Martel, J. Appenzeller, P. Avouris, Appl. Phys. Lett. **80** 2773 (2002)
42. M. Shiraishi, K. Takebe, K. Matsuoka, K. Saito, N. Toda, J. Appl. Phys. **101** 014311 (2007)
43. S. Kalinin, D.B. Bonnell, M. Freitag, A.T. Johnson, Appl. Phys. Lett. **81** 754 (2002)
44. Y. Miyato, K. Kobayashi, K. Matsushige, H. Yamada, Jpn. J. Appl. Phys. **44** 1633 (2005)
45. Y. Miyato, K. Kobayashi, K. Matsushige, H. Yamada, Nanotechnology **18** 084008 (2007)
46. J. Appenzeller, J. Knoch, V. Derycke, R. Martel, S. Wind, P. Avouris, Phys. Rev. Lett. **89** 126801 (2002)
47. S. Heinze, J. Tersoff, R. Martel, V. Derycke, J. Appenzeller, P.h. Avouris, Phys. Rev. Lett. **89** 106801 (2002)

48. D. Brunel, D. Deresmes, T. Mélin, Appl. Phys. Lett. **94** 223508 (2009)
49. M. Radosavljevic, M. Freitag, K.V. Thadani, A.T. Johnson, Nano Lett. **2** 761 (2002)
50. B. Babic, M. Iqbal, C. Schönenberger, Nanotechnology **14** 327 (2003)
51. T. Umesaka, H. Ohnaka, Y. Ohno, S. Kishimoto, K. Maezawa, T. Mizutani, Jpn. J. Appl. Phys. **46** 2496 (2007)
52. W. Kim, A. Javey, O. Vermes, Q. Wang, Y. Li, H. Dai, Nano Lett. **3** 193 (2003)
53. M.S. Fuhrer, B.M. Kim, T. Durkop, T. Brintlinger, Nano Lett. **2** 755 (2002)
54. A. Stirling, A. Pasquarello, J.C. Charlier, R. Car, Phys. Rev. Lett. **85** 2773 (2000)